Flood-Related Extreme Precipitation in Southwestern Germany: Development of a Two-Dimensional Stochastic Precipitation Model

Florian Ehmele[1] and Michael Kunz[1,2]

[1]Institute of Meteorology and Climate Research, Karlsruhe Institute of Technology (KIT), Hermann-von-Helmholtz-Platz 1, 76344 Eggenstein-Leopoldshafen, Germany.
[2]Center for Disaster Management and Risk Reduction Technology (CEDIM), KIT - Karlsruhe, Germany

Correspondence to: Florian Ehmele (florian.ehmele@kit.edu)

Abstract. Various fields of application, such as risk assessments of the insurance industry or the design of flood protection systems, require reliable precipitation statistics in high spatial resolution, including estimates for events with high return periods. Observations from point stations, however, lack of spatial representativeness, especially over complex terrain. Current numerical weather models are not capable of running simulations over thousands of years. This paper presents a new method for the stochastic simulation of widespread precipitation based on a linear theory describing orographic precipitation and additional functions that consider synoptically driven rainfall and embedded convection in a simplified way. The model is initialized by various statistical distribution functions describing prevailing atmospheric conditions such as wind vector, moisture content, or stability, estimated from radiosonde observations for a limited sample of observed heavy rainfall events. The model is applied for the stochastic simulation of heavy rainfall over the complex terrain of Southwest Germany. It is shown that the model provides reliable precipitation fields despite its simplicity. The differences between observed and simulated rainfall statistics are small, being in the order of only $\pm\,10\,\%$ for return periods of up to 1,000 years.

1 Introduction

Severe pluvial flood events resulting from persistent rainfall over large areas has the potential to cause high economic losses of several billion euros (EUR) in central Europe. In Germany, the two extreme floods of 2002 and 2013 with estimated return periods of more than 200 years (Schröter et al., 2015) resulted in losses of more than EUR 22 billion (inflation adjusted to 2017; MunichRe, 2017). In addition to these rare extreme events, less severe floods with shorter return periods, such as in 2005, 2006, 2010, and 2011 (Uhlemann et al., 2010; Kienzler et al., 2015), also contribute significantly to the large average annual losses from floods of EUR 1.1 billion in Germany in the last 30 years (MunichRe, 2017). Flood risk estimation, for example, for insurance purposes or for the design of appropriate flood protection systems, requires comprehensive statistical analyses of both runoff and rainfall. Traditionally, extremes associated with the latter have been estimated at point stations from intensity-duration-frequency (IDF) with extreme value statistics being applied (Koutsoyiannis et al., 1998). This method, however, implies two major difficulties: (i) the low density of point observations and their limited representativeness in particular over complex terrain, and (ii) the limited observation period with the consequence that not all possible extreme configurations enter the samples.

To account for the former issue, geostatistical interpolation routines, such as kriging (Goovaerts, 2000), or techniques relating precipitation and orographic or atmospheric characteristics (e.g., Basist et al., 1994; Drogue et al., 2002) have been applied. Recently, Marra et al. (2017) showed that IDFs can be reliably estimated from remote sensing data, such as weather radars, with high spatial coverage. However, the conversion from radar reflectivity to rain intensity leads to high uncertainty mainly because of the unknown drop size distribution in combination with the radar reflectivity being proportional to the drop diameter in the sixth power. Comparing IDFs obtained from radar data with point observations on a local scale, Peleg et al. (2018) found that the spatial IDFs tend to underestimate rainfall intensity for short return periods, and that the natural variability of extreme rainfall increases the uncertainties of the IDFs for longer return periods and larger areas.

To account for the limited observation period, several studies have employed stochastic weather generators to simulate precipitation events at single grid points (e. g., Richardson, 1981; Furrer and Katz, 2007; Neykov et al., 2014). A recent study by Cross et al. (2017), for example, introduced a censored rainfall modeling approach designed to reduce the underestimation of extremes. Albeit considering the long-term variability of precipitation, which leads to more reliable estimates for extremes, these approaches still lack spatial representativeness.

Furthermore, robust estimates of precipitation extremes with high return periods, for example, for a one-in-200-year event, require a large sample size of several thousands of events. Current numerical weather prediction (NWP) models, though having a high spatial resolution of several kilometers, are not able to simulate thousands of events due to their complexity and the resulting high computing costs.

In this study we present a two-dimensional stochastic precipitation model (SPM2D), which was designed for the stochastic simulation of a very large number of precipitation fields in high spatial resolution. Precipitation associated with different processes such as orographically-induced wave dynamics, large-scale lifting, or embedded convection is described by simplified parameterizations and combined linearly. Inclusion of several physically based tuning parameters of the model helps to keep track to precipitation patterns of real events. The model relies on several input parameters such as wind speed and direction, static stability, or moisture obtained from radiosoundings. By doing so, the input parameters have to keep constant over the whole investigation area and for time period of the soundings, usually 12 hours. For the stochastic simulations, these input parameters are varied randomly based on appropriate probability density functions (pdfs) derived from a representative sample of historical heavy rainfall events. Because precipitation regimes in summer and winter vary significantly, we seasonally differentiate our analyses. The SPM2D is one component of a novel risk assessment method to quantify the probable maximum loss for a 200-year event (PML200) by considering simultaneous flooding along the main river networks. This paper, however, discusses only on the precipitation/hazard component.

The paper is structured as follows: Section 2 introduces the basic concept of the SPM2D. Section 3 briefly describes the data sets used in this study. Section 4 presents the results of the calibration based on a set of 200 representative historical heavy rainfall events and examines sensitivities of the model depending on varying ambient conditions. Section 5 shows some characteristics of the selected events. Results of the stochastic simulations are discussed in Section 6, and Section 7 lists some conclusions. Further information are given in a short appendix and supplementary material.

2   Stochastic Precipitation Model

The SPM2D model is designed for the simulation of widespread, pluvial precipitation over complex terrain such as low mountain ranges, a typical feature of European topography. The investigation area for this study is the Federal State of Baden-Württemberg (BW) in Southwest Germany (Fig. 1). The terrain exhibits a certain degree of complexity with the broad Rhine Valley with elevations of 100–200 m bounded by the Vosges Mountains (France) to the west and the Black Forest mountains to the east. The highest peak is the Feldberg with a maximum elevation of 1493 m in southern Black Forest. To the northeast, the topography is more flat with some rolling terrain. Annual precipitation varies between 600 mm (southern Rhine Valley) and approximately 2000 mm (southern Black Forest).
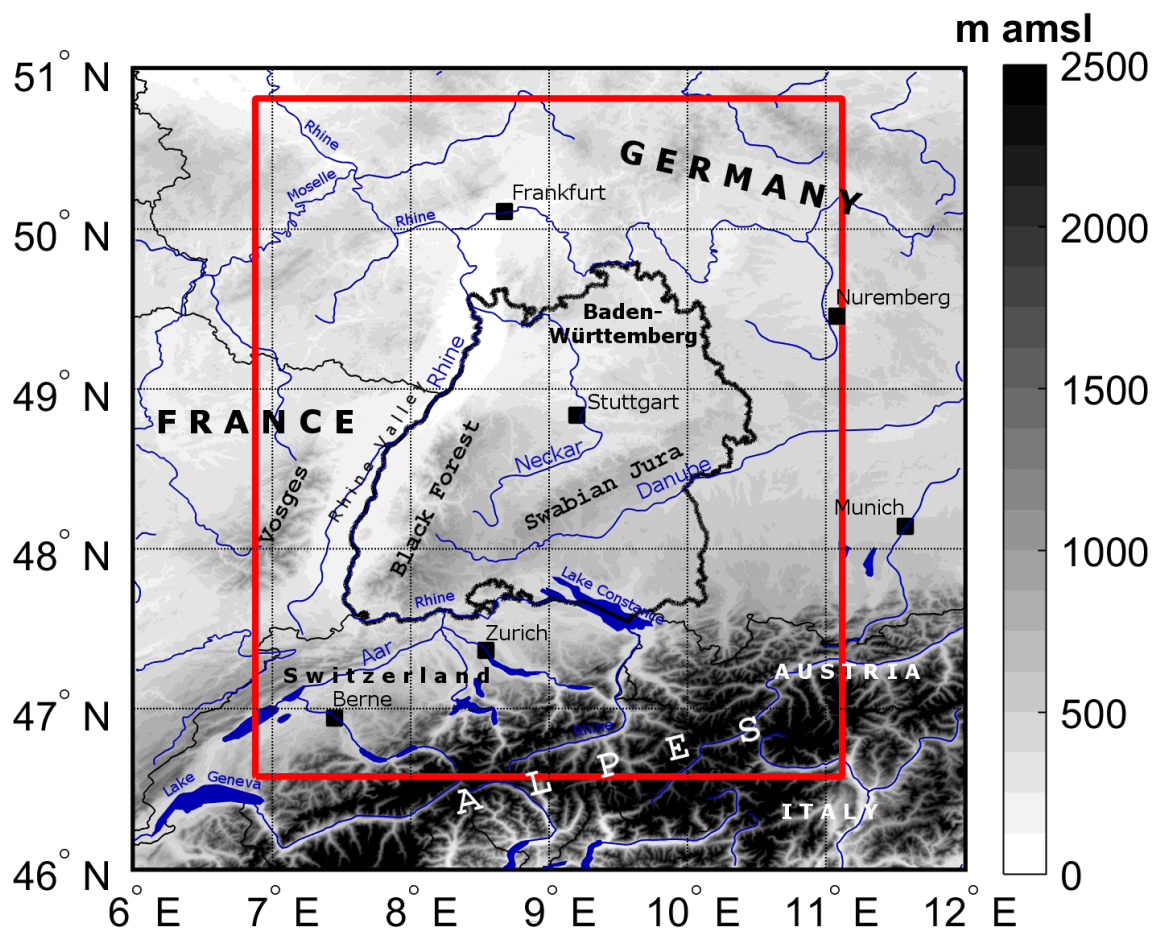
Figure 1. Topographic map of Southwestern Germany and surrounding areas with main river networks and lakes as well as substantial orographic structures. The national borders (slim solid black contours) and the border of the Federal State of Baden-Württemberg (bold solid black contour) are shown as well as the model domain (red box), which extends from 46.6 to 50.8° N and from 6.9 to 11.1° E.

As described in the following Sect. 2.2, orographic precipitation is computed in Fourier space, and therefore, the model domain has to be symmetric with 2^n (n is a positive integer). In this study we used a 512×512 grid with a resolution of $1 \, \text{km}^2$. Also note that the assumption of horizontal homogeneous conditions, which is a prerequisite for the orographic model, limit the overall size of the model domain.

5   After a description of the model components (Sect. 2.1 – 2.3), some necessary preparations and an overview of the general simulation procedure are presented in Sect. 2.4.

2.1   General description

Overall, the model SPM2D quantifies total precipitation R_{tot} from the linear superposition of four terms, each of them representing a specific precipitation process:

$$R_{\text{tot}} = R_{\text{oro}} + R_\infty + R_{\text{front}} + R_{\text{conv}} \,. \tag{1}$$

The first two components of Eq. (1) originate from the diagnostic linear model of orographic precipitation according to Smith and Barstad (2004) and Barstad and Smith (2005), hereafter referred to as Smith-Barstad-Model (SBM). The first component, R_{oro}, quantifies rain enhancement as a consequence of orographically induced lifting. Over complex terrain and for high amounts of incoming water vapor flux (Kunz, 2011), this part dominates the other three in (Eq. 1). The next term, R_∞, is the
15   background precipitation related to synoptic-scale lifting. According to the ω-equation, large-scale lifting, preferably occurring downstream of troughs (low pressure systems at higher levels), is the result of three different mechanisms: positive vorticity advection increasing with height (or vice versa); maximum of diabatic phase transitions; and maximum of warm air advection. Even though lifting results from the superposition of these three mechanisms, we do not split R_∞ accordingly, as the single forcing terms cannot be estimated from vertical soundings used as input data in our approach (see Section 3.2).

20   As the SBM does not reliably reproduce the observed spatial variability of precipitation also over flat terrain for physical reasons (Kunz, 2011), we have implemented two additional components: R_{front} to consider precipitation associated with synoptic-scale fronts, and R_{conv} related to embedded convection atop of stratiform clouds on a local scale (e.g., Fuhrer and Schär, 2005; Kirshbaum and Smith, 2008). While the former component can modify the entire precipitation field, the latter can lead to enhanced totals on the local scale. Deep moist convection, however, is not considered as it is not relevant for larger river
25   floods. Note that both R_{oro} and R_{front} can attain negative values in descent areas. Negative values of total precipitation R_{tot}, however, are physically not meaningful and are therefore truncated away (i.e., $R_{\text{tot}} = \max(R_{\text{tot}}, 0)$ in Eq. 1).

2.2   The Smith-Barstad Model (SBM)

The linear orographic model SBM (Smith and Barstad, 2004; Barstad and Smith, 2005) is a simple yet efficient way to compute precipitation over complex terrain. It has been successfully applied in various regions around the world: e. g. several locations
30   in the United States (Barstad and Smith, 2005), Iceland (Crochet et al., 2007), Southwest Germany (Kunz, 2011), or Southern and Northern Norway (Caroletti and Barstad, 2010; Barstad and Caroletti, 2013).

2.2.1 Orographic precipitation

The SBM is based on the linear theory of three-dimensional (3D) stratified, hydrostatic flow over mountains with uniform incoming horizontal wind speed and stability (Smith, 1980, 1989). It explicitly considers linear flow effects evolving over mountains, such as upstream-tilted gravity waves or flow that goes around rather than over an obstacle in the case of low wind speed, high static stability, and/or large mountains (i. e. small Froude numbers). It is assumed that saturated lifting produces condensed water that falls to the ground after a certain time shift (Jiang and Smith, 2003). Thus, precipitation on the ground is directly related to the condensation rate.

One of the key components of the linear model is a pair of linear steady-state equations for the advection of vertically integrated cloud water and hydrometeor density during characteristic time scales of cloud water conversion τ_c and the fallout of hydrometeors τ_f respectively. Both time scales are mathematically analogous and are assumed to be constant in time and also in space for mesoscale domains. When the time scales are set to zero, the maximum precipitation is almost one order of magnitude larger compared to a configuration with, for example, $\tau_f = \tau_c = 1000$ s (Kunz, 2011).

A powerful method for the solution of the advection equations for cloud physics together with 3D flow is to apply a two-dimensional (2D) Fourier transform. Precipitation at the ground is obtained via an inverse FFT given by the transfer function:

$$R_{\mathrm{oro}}(x,y) = \iint \frac{iC_{\mathrm{w}}\sigma\hat{h}(k,l)}{(1-imH_{\mathrm{w}})(1+i\sigma\tau_c)(1+i\sigma\tau_f)} \cdot \mathrm{e}^{i(kx+ly)}\mathrm{d}k\mathrm{d}l\,, \tag{2}$$

which connects the precipitation field in Fourier space (fraction term) to the orography, $\hat{h}(k,l)$, both related to the horizontal wavenumbers (k,l); i is the imaginary unit, and $C_{\mathrm{w}} = \rho_{\mathrm{S_{ref}}}\Gamma_{\mathrm{m}}\gamma^{-1}$ is the uplift sensitivity related to the condensation rate $\rho_{\mathrm{S_{ref}}} = \rho_{\mathrm{d}}q_{\mathrm{v}}$, where ρ_{d} is the density of dry air, q_{v} is the water vapor density, and Γ_{m} and γ are the moist adiabatic and actual lapse rates, respectively. The water vapor scale height H_{w} is the (absolute) height where the integrated water vapor density dropped to e^{-1}, and $\sigma = Uk + Vl$ is defined as the intrinsic frequency with the components U and V of the undisturbed horizontal wind vector assumed to be constant through time and space.

Whereas the nominator of Eq. (2) gives the dependency of precipitation on vertical motion and orography, the first bracket of the denominator describes the modification of the source term by airflow dynamics. The second and third terms of the denominator consider the advection of hydrometeors during the characteristic time scales τ_{x} ($x = c; f$). In case of descent downstream of mountains, R_{oro} may become negative leading to a reduction of total precipitation in Eq. (1) in that area.

The vertical wavenumber m in Eq. (2) is given by the dispersion relation (Smith, 1980):

$$m(k,l) = \left[\frac{N_{\mathrm{m}}^2 - \sigma^2}{\sigma^2}(k^2 + l^2)\right]^{0.5}. \tag{3}$$

In this formulation, m controls both the depth and tilt of forced ascent or descent. Because vertical lifting is assumed to be saturated throughout the whole column, meaning that the lifted condensation level (LCL) is directly at the ground, saturated Brunt-Väisälä frequency N_{m} (e. g., Lalas and Einaudi, 1973) has to be considered instead of the dry one, N_{d}. Compared to unsaturated conditions, saturated flow leads to a weakening of the amplitude of the gravity waves via the reduction of

static stability. In this case, the flow tend to go more directly over an obstacle rather than around (Durran and Klemp, 1982; Kunz and Wassermann, 2011). Even though the concept of saturated flow by simply considering N_m must be regarded as an approximation of the reality, it has been successfully applied by several authors studying flow dynamics and precipitation (Jiang and Smith, 2003; Smith and Barstad, 2004; Kunz and Wassermann, 2011).

5   Combining Eq. (2) with (3), a total number of seven atmospheric parameters is required as input for R_{oro}. In this study, we used vertical profiles of temperature, moisture, and wind from radiosoundings (see Sect. 3.2) for that purpose.

2.2.2 Background precipitation

Under the assumption that the prevailing synoptic conditions during the 12 hours of model integration are approximately horizontally homogeneous and stationary, also R_∞ becomes constant. To consider large-scale lifting in the SPM2D, we estimate

10   R_∞ from observed rainfall totals (see Sect. 3.1) over a larger area with almost flat terrain, where R_{oro} as well as evaporation associated with ascent are minimized to a large degree. To ensure proper estimation of R_∞ for the historic events, we choose an area that covers most of the total investigation area, but excludes the Black Forest and the Prealpine region, where precipitation totals are highest. In the selected region (Fig. 2, black box), large totals occur only rarely. Values of more than 50 mm per day, for example, exhibit an annual exceedance probability p of less than 0.5. Furthermore, as confirmed by Fig. 2, the probability

15   of rain totals in excess of 50 mm per day is more or less homogeneously distributed.
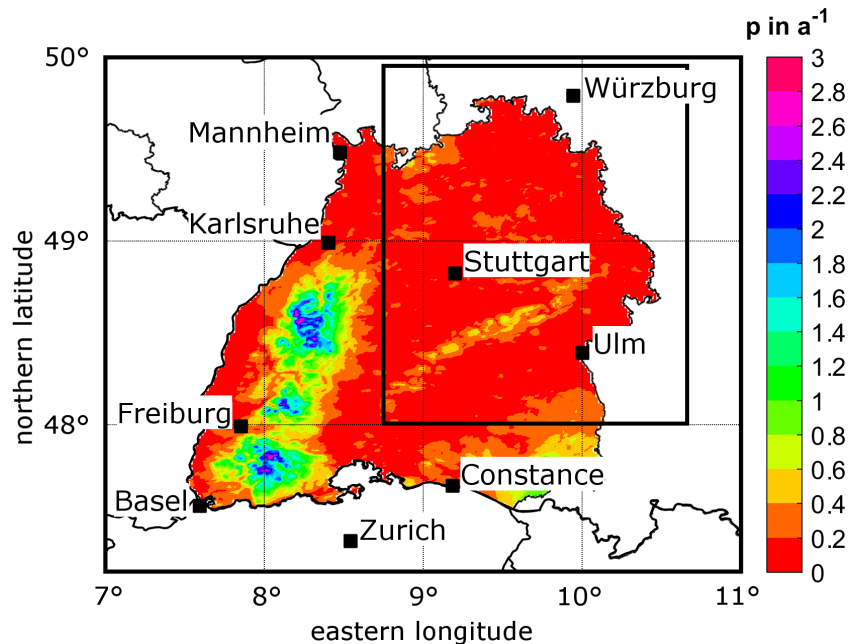
Figure 2. Probability of observed 24-hour rainfall totals greater than 50 mm expressed as the average days per year for Baden-Württemberg; the black box indicates the area, where background precipitation R_∞ is estimated.

2.3 Modifications of the SBM

As further development, two types of modifications are applied to the SBM: adjustments to the existing orographic precipitation using additional calibration parameters, and additional precipitation components originating from different physical processes.

2.3.1 Adjustments to R_{oro}

The original orographic precipitation equation of the SBM (2) is modified in SPM2D by adding three constant calibration parameters (bold symbols):

$$R_{oro}(x,y) = \boldsymbol{c_{oro}} \cdot \boldsymbol{f_{dry}}(\boldsymbol{x},\boldsymbol{y}) \cdot \iint \frac{i\boldsymbol{f_{C_w}}C_w\sigma\hat{h}(k,l)}{(1-imH_w)(1+i\sigma\tau_c)(1+i\sigma\tau_f)} \cdot e^{i(kx+ly)}dkdl. \tag{4}$$

The uplift sensitivity factor C_w is adjusted by a multiplier f_{C_w}, which reduces the sensitivity of the SPM2D for lifting and therefore, the precipitation rate. Precipitation is reduced the most for sharp height gradients, whereas the effect is only weak for smooth terrain (Fig. 3, red curve). The formulation of SPM2D also allows for multiple ascents/descents of a virtual air parcel without any changes in its water vapor content. The more realistic partial removal of water vapor due to condensation during ascent is also considered by implementing the additional function f_{C_w}.

An additional parameter, f_{dry}, is implemented in Eq. (4) to reduce evaporation in descent regions, where R_{oro} becomes negative (Fig. 3, blue curve). The resulting underestimation of precipitation is found especially downstream of steeper mountains with greater descent (Kunz, 2011). The parameter $f_{dry} < 1$ only corrects grid points (x,y) where $R_{oro} < 0$; otherwise $f_{dry} = 1$.
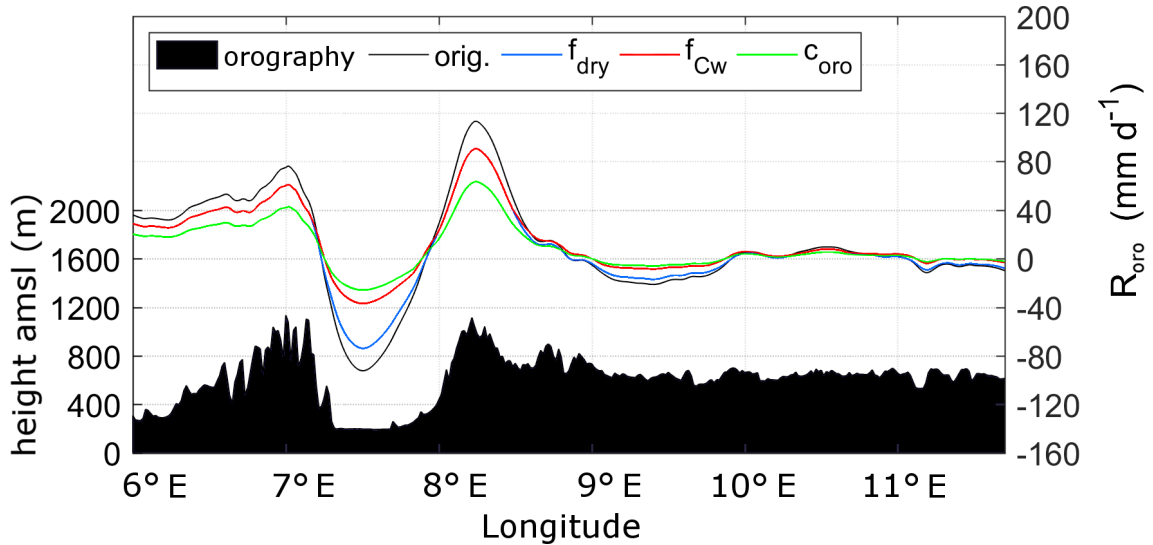
Figure 3. Different effects of the implemented internal free parameters f_{dry} (blue), f_{C_w} (red) and c_{oro} (green) on the original orographic precipitation part (black curve) for a west-to-east cross section through the model domain. The underlying orography is shown in black.

Finally, the last additional calibration parameter, c_{oro}, reduces orographic precipitation in the whole domain (Fig. 3, green curve). It is a consequence of the assumption that the vertical lifting of an air column with overall saturation produces condensate and instantaneous fallout at any time, implying an overestimation of precipitable water. In reality, not all layers are completely saturated, and water may also partly be stored by clouds. The parameter c_{oro} is assumed to be independent of any lifting processes and constant in time and for the whole domain. From a mathematical perspective, the two factors, f_{C_w} and c_{oro}, could collapse to one single parameter. Nevertheless, as mentioned above, they describe modifications of different physical processes and must therefore remain separate.

2.3.2 Frontal precipitation

Apart from large-scale lifting connected to low-pressure systems or waves in the flow patterns, precipitation is also substantially enhanced by synoptic-scale weather fronts. Active fronts may increase precipitation considerably due to cross-frontal circulations and lifting in the warm sector of a cyclone (e. g., Bergeron, 1937; Eliassen, 1962). Conversely, if a front affects only parts of the investigation area (e.g., in case of a trailing front, where the flow is almost parallel to the isobars), regions not affected by the front experience much less or even no rain at all. Both effects are considered by a simplified parameterization R_{front} in Eq. (1):

$$R_{front} = (R_{oro} + R_\infty) \cdot (c_{front} - 1), \tag{5}$$

where c_{front} serves as an enhancement or reduction factor of the overall precipitation. In this parameterization, R_{oro} is considered again because frontal precipitation is additionally enhanced by orography as shown, for example, by Browning et al. (1975) or Houze and Hobbs (1982). Due to the additive superposition of all precipitation components in Eq. (1), we have to subtract the original precipitation totals leading to a total multiplier of $(c_{front} - 1)$.

In order to estimate c_{front} from the observational data, we define this quantity as the relative difference between observations O and output M of the SBM. This is expressed by

$$c_{front} = \overline{O} \cdot \overline{M}^{-1} \tag{6}$$

assuming that the differences originate primarily from frontal effects. For the quantification of c_{front}, we use spatial mean values over the investigation area $\overline{O}$ and $\overline{M}$ for a training sample of historic heavy rain events (see Sect. 2.4.1).

The frontal enhancement factor is a function of space realized by a rectangular area $c_{front}(n, t)$, where the orientation of the front-parallel t-axis compared to the zonal-orientated y-axis is prescribed by the mean wind direction β (Fig. 4). For each time step the maximum value of c_{front} is estimated using the corresponding pdf (c. f. Sect. 5.1). To avoid strong gradients at the borders of the rectangular, we applied Gaussian-shaped smoothing: Along the front-normal n-axis, the spread is set to $8\sigma_n$, where σ_n is the standard derivation of the normal distribution; in the t-direction, the front is infinitely extended (Fig. 4). As the minimum of c_{front} is zero, R_{front} can also attain negative values, leading to a weakening of total precipitation for areas unaffected by a front.
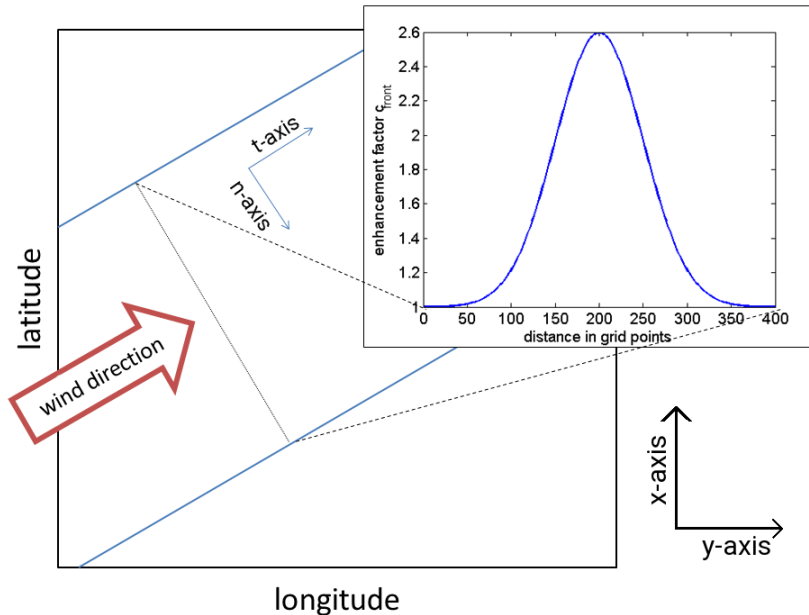
Figure 4. Schematic of a Gaussian-shaped distribution of the frontal enhancement factor with a maximum of $c_{\text{front}} = 2.6$ and $\sigma_n = 50$ (upper right corner) and its location in the model domain for a southwesterly wind direction (arrow). The blue lines indicate the boundaries of the frontal zone.

2.3.3 Embedded Convection

Embedded convection mainly occurs when lifting is locally enhanced at mid- and upper tropospheric levels leading to a decrease of thermal stability by the release of latent heat of condensation (e. g., Kirshbaum and Durran, 2004; Kirshbaum and Smith, 2008; Cannon et al., 2012). Convection in general involves several complex processes that makes reliable simulations a difficult task. Since our model is restricted to large-scale precipitation with the objective of quantifying extremes of areal precipitation solely, we treat embedded convection in a very simplified way by implementing several rectangular cells as convective footprints similar to the approach for the fronts.

Because embedded convection is mainly induced by orographic lifting, we implemented a multiplicative factor to the precipitation fields related to both orographic and large-scale lifting, similar to the frontal part:

$$R_{\text{conv}} = c_{\text{conv}} \cdot (R_{\text{oro}} + R_{\infty}), \tag{7}$$

with the enhancement factor c_{conv}. For each 24-hour simulation period, we choose a number of rectangular convective footprints, each with a specified width W and length L, and distribute them randomly over the whole model domain (Fig. 5). The dimensions for each rectangle are estimated from the pdfs of historic footprints of deep moist convection (see Sect. 3.3). Furthermore, we restricted the two parameters to $L > W$ and $L_{\text{max}} = 300$ km, or 300 grid points, respectively. As for the frontal
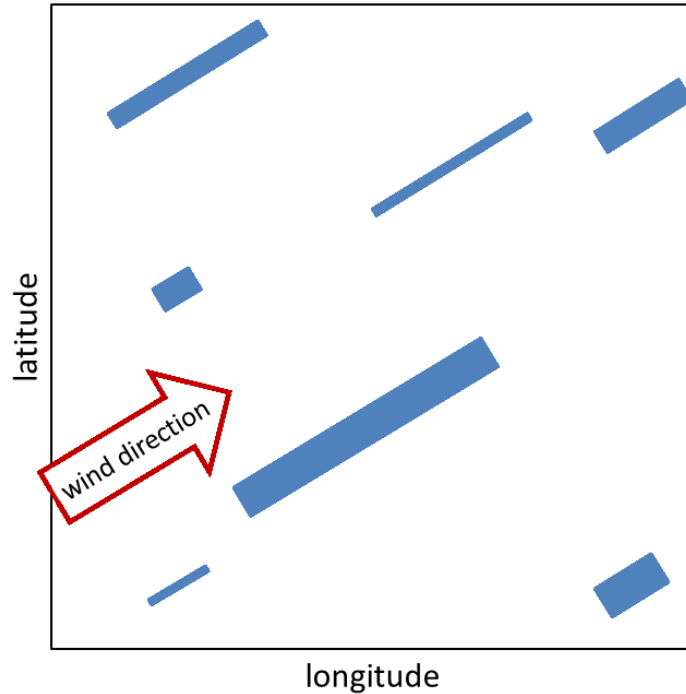
Figure 5. Schematic of embedded convection implementation by using rectangular cells (blue). The orientation is defined by the wind direction (arrow); each cell is assigned to an individual factor c_{conv}.

systems, the wind direction defines the orientation of the longer sides of the rectangles. For each footprint, we choose $L \cdot W$ specific factors c_{conv} with $c_{\mathrm{conv}} \in \{0; 1\}$. As found, for example, by Fuhrer and Schär (2005) or Cannon et al. (2012), embedded convection can enhance precipitation up to $200\,\%$, but only locally. Thus, the given range of c_{conv} is adequate. Within the single rectangles, the spatial distribution of c_{conv} randomly varies between the given limits to account for the high spatial variability of convective precipitation.

As embedded convection occurs several times a day and at several locations, we used a variable number of convective footprints in the model. The complete convective precipitation field for each time step is spatially smoothed to avoid sharp gradients. For this, we applied a moving average of 10 grid points to preserve the high spatial variability of convection.

2.4 Pre-Preparations and Simulation Procedure

2.4.1 Event definition and statistical distribution functions

Stochastic modeling of precipitation events with the SPM2D is based on appropriate pdfs of all input parameters required by the model. These pdfs are estimated using an adequate set of representative past heavy rainfall events. Because the characteristics of

the ambient conditions and thus the precipitation regimes change throughout the year, we seasonally differentiate the estimated pdfs between spring (March-April-May, MAM from hereon), summer (June-July-August, JJA), autumn (September-October-November, SON), and winter (December-January-February, DJF).

In the first step, a sufficient and appropriate subset of relevant historic events was identified. Here, an event is defined as a period of one or more days with persistent precipitation above a certain threshold of daily totals. An extension to multi-day events is reasonable to consider time delays in discharge response or flood waves traveling along river networks (e. g., Duckstein et al., 1993; Uhlemann et al., 2010; Schröter et al., 2015).

We define the historic event set according to maximum areal precipitation. For this, we simply accumulate the (equidistant) 24-hour rainfall totals $\overline{R}_{\mathrm{BW}}$ of all grid points in the investigation area (BW; see Sect. 3.1). Following the sorting of all values of $\overline{R}_{\mathrm{BW}}$ in descending order, the strongest 200 values enter the sample (top200). As precipitation is not limited to these (single) days but may be embedded in longer time periods, we define the threshold R_{thres} for the event definition. For estimating R_{thres}, we consider "wet" days by using $\overline{R}_{\mathrm{BW}} > 0$ solely, and set R_{thres} to the 75 % percentile of this sub-sample. A lower threshold leads to an over-interpretation of longer clusters, a higher one avoids multi-day events.

Event precipitation starts on the first day that exceeds R_{thres}. When areal means of consecutive days are also above R_{thres}, they are simply accumulated, yielding events of more than one day. The last day with $R \geq R_{\mathrm{thres}}$ before a period of at least three days of non-exceedance defines the end of an event. Such a three-day period ensures statistical independence of the events in accordance with the approach of Palutikov et al. (1999) for wind storms. Following Piper et al. (2016), we only count "rain days" ($\overline{R}_{\mathrm{BW}} \geq R_{\mathrm{thres}}$) and neglect "skip days" ($\overline{R}_{\mathrm{BW}} < R_{\mathrm{thres}}$) in between the start-day/end-day period for event duration estimation, which is a widely used approach (Wanner et al., 1997; Petrow et al., 2009). This approach avoids the over-interpretation of longer clusters. Based on this procedure, a defined precipitation event contains one or more days of the top200 sample. For this event set, all required input parameters were extracted from sounding data and rainfall totals (see Sect. 3).

In the next step, we identified the pdfs most appropriate for statistically describing each of the seven atmospheric input parameters, event duration t_{ev}, background precipitation R_{∞} and front factor c_{front}. In addition to 20 pdfs preset by the MATLAB statistic toolbox (MATLAB, 2016), we considered the circular von-Mises distribution (Mardia and Zemroch, 1975) for wind direction only. In Sect. 5 it will be further discussed which pdfs are most suitable for the input variables in our case.

To find the pdf that best fits the data, we estimated the appropriate number of histogram classes according to Freedman and Diaconis (1981), and calculated bias, root mean square error (rmse) and Spearman correlation coefficient r_{Sp} (Spearman, 1904) as quality indicators (QIs). We also applied a χ^2-test (Wilks, 2006) as a QI. For each QI, we ranked the pdfs in ascending order and added up the rank numbers for each pdf, receiving the best fit in terms of the least QI–rank sum (QIRS). In the case of alikeness of two or more pdfs (about 10 % of all cases), we manually selected the best one.

2.4.2 General Simulation Procedure

The presented SPM2D is an event-based model in the sense that a specified number n_{E} of independent events with variable duration t_{ev} is simulated. The general procedure is as follows (cf. Fig. 6): Starting with the iteration loop over n_{E} events, the season and duration t_{ev} are set at first. The next step is the simulation of the four precipitation components according to Eq. (1);
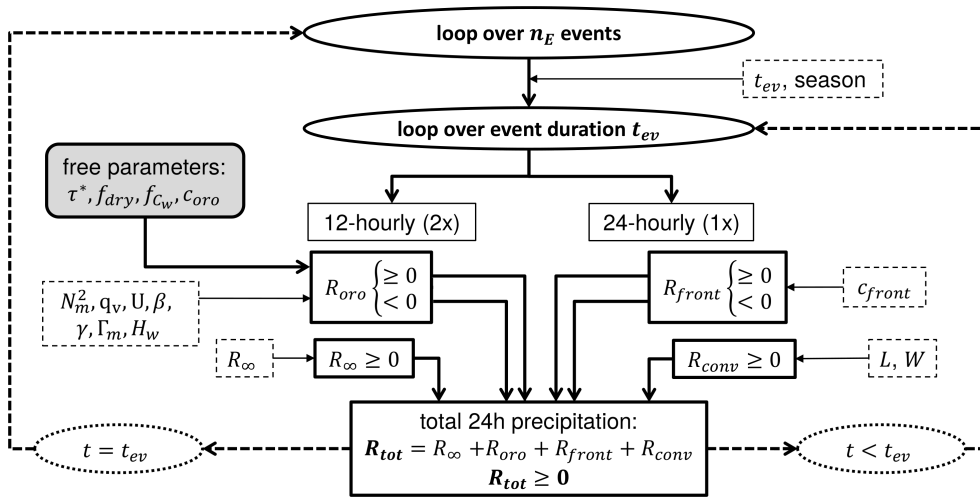
Figure 6. Flow chart of the individual components of the SPM2D (solid boxes) and the corresponding input variables (pdfs; dashed boxes). Loops are highlighted as ellipsis or bold dashed arrows. The constant model parameters are illustrated as shaded box.

because radiosoundings used as input data are available every 12 hours, R_{oro} and R_∞ are computed for the same period. In contrast, R_{front} and R_{conv} are calculated only for 24 hours as they become apparent as footprints in daily totals. The resulting total precipitation R_{tot} has a temporal resolution of 24 hours. Despite the fact that the characteristic time scales may vary from one situation to another, it is found that simulations using fixed values for the free parameters yield trustworthy results (e. g.

5 Barstad and Smith, 2005; Kunz, 2011). Here, we also use constant values illustrated as shaded box in Fig. 6. The direct link between the precipitation components and the corresponding input variables (described by appropriate pdfs) is also shown in Fig. 6. In case $t < t_{\mathrm{ev}}$, the next 24-hour period is simulated; otherwise, the loop jumps to the next event. A method how to assign the n_{E} events to a specific time period, which is required, for example, for insurance purposes, will be introduced in Sect. 6.

10 3 Data sets

The SPM2D presented in this study is based on two different types of data sets: gridded precipitation data also used to calibrate and verify the model, and vertical profiles from radiosondes to initialize the model. Furthermore, the SPM2D is also validated using reanalysis.

3.1 Rainfall totals

15 Rainfall statistics in our study are based on the regionalized precipitation (REGNIE) data provided by the German Weather Service (DWD). REGNIE is a gridded data set of 24-hour totals (06 to 06 UTC) based on several thousand climate stations more or less evenly distributed across Germany (so-called RR collective). The REGNIE algorithm interpolates the observations to a

regular grid of $1\,\mathrm{km^2}$ considering elevation, exposition, and climatology (Rauthe et al., 2013). Despite of continuous changes in the number of stations considered and several station relocation, REGNIE is sufficiently homogeneous for our purposes. However, areal precipitation exhibits a certain bias especially over elevated terrain, such as the peaks of Black Forest, where the number of stations is very limited (Kunz, 2011).

5   In our study, we use REGNIE data between 1951 and 2016 to identify the top200 event set (see previous section), to estimate the duration of the events, the front factor c_{front}, and background precipitation as well as for the validation of the SPM2D simulation results.

3.2   Radiosoundings

The seven input parameters (see Sect. 2) required by the SPM2D model are derived from vertical profiles (00 and 12 UTC)
10 of temperature, moisture, wind speed, and direction at the radiosounding station of Stuttgart located somewhat downstream of the northern Black Forest. Even though the location might not be ideal because the profiles do not represent undisturbed conditions, the profiles are similar to those of the upstream station of Nancy in France as shown by Kunz (2011) for heavy rainfall events on average. Data from Nancy are available after 1990 only and, thus, cannot be used in this study, whereas soundings from Stuttgart are available since 1957.

15   The vertical profiles, provided by the Integrated Global Radiosonde Archive (IGRA) from the National Climatic Data Center (Durre et al., 2006), were interpolated into equidistant increments of $\Delta z = 10\,\mathrm{m}$ (Mohr and Kunz, 2013). All derived environmental parameters refer to the lowest $5\,\mathrm{km}$ of the atmosphere since this layer is most relevant for air flow and stability. Furthermore, to account for the decreasing impact of higher atmospheric layers on the flow characteristics, the flow parameters Λ are integrated vertically ($\widetilde{\Lambda}$) applying water vapor weighting (Kunz, 2011):

$$
20 \quad \widetilde{\Lambda} = \frac{\int_{z=0}^{z_{\mathrm{t}}} \Lambda \rho_{\mathrm{d}} q_{\mathrm{v}}\, dz}{\int_{z=0}^{z_{\mathrm{t}}} \rho_{\mathrm{d}} q_{\mathrm{v}}\, dz}, \tag{8}
$$

where ρ_{d} is the density of dry air and z_{t} is the upper integration limit, here of $5{,}000\,\mathrm{m}$. As some layers may be moist-unstable, resulting in imaginary N_{m}, the averaging routine is applied to N_{m}^2. In the few cases, where $\widetilde{N}_{\mathrm{m}}$ was imaginary, it was set to a near-neutral, constant value of $0.0003\,\mathrm{s^{-1}}$.

3.3   Parameters for Embedded Convection

25 The stochastic generation of enhanced precipitation streaks associated with embedded convection, namely their length and width (L and W), rely on the statistics of severe convective storms in Germany (Fluck, 2018). In that study, convective storms in Germany, France, Belgium, and Luxembourg between 2005 and 2014 were identified from the constant altitude plan position indicator (CAPPI) for a reflectivity in excess of $55\,\mathrm{dBZ}$. The application of the tracking algorithm TRACE3D (Handwerker, 2002) identified more than 25,000 storm tracks. Even though we do not consider rainfall related to severe convective storms in
30 the SPM2D, the statistical distributions of the storm's dimensions are reliable proxies for the extension of enhanced precipitation from embedded convection described by R_{conv}.

3.4 Numerical Weather Simulations

The SPM2D simulation results are additionally validated with high-resolution reanalysis from the non-hydrostatic Consortium for Small-scale Modeling (COSMO) model in climate mode (CCLM; Rockel et al., 2008). Laube (2018) performed a dynamical downscaling of ERA-40 reanalysis from the European Center for Medium-Range Weather Forecasts (ECMWF; Kållberg et al., 2004) to a horizontal resolution of 2.8 km for Southern Germany using a threefold regional nesting (50, 7, to 2.8 km). High-resolution CCLM data is available for the period 1971–2000. For the evaluation, we considered the top200 REGNIE events, from which around 100 events occurred within the CCLM period including the top two and 7 (14) of the strongest 10 (20) events.

4 Calibration

4.1 Method

The SPM2D is calibrated with the top200 events (training data) by adjusting the free model parameters τ_x, $f_{\mathrm{C_w}}$, f_{dry} and c_{oro} (cf. Sect. 2) and comparing the simulation results with observations. The parameter combination yielding the best simulation results are then used for the stochastic simulations (validation data). The components R_{front} and R_{conv} are only considered for the stochastic event set and therefore neglected here. In this configuration, the SPM2D is equivalent to the SBM plus our modifications in R_{oro}, referred to as SBM+M.

In order to determine appropriate values of the free parameters, a large number of model simulations was carried out. Whereas one parameter was successively varied, the others were kept constant. The selected ranges and increments of the parameters listed in Table 1 resulted in 2,016 possible parameter combinations, giving a total number of approximately 390,000 simulation days for the top200 event set. Both data sets (from SBM+M and REGNIE) are slightly smoothed using a running 5×5 grid box as the REGNIE data show a certain spatial uncertainty (c. f. Sect. 3.1) especially around the crests of Black Forest. Furthermore, as shown, for example, by Barstad and Smith (2005), smoothed data yield more robust results when comparing model and observation data. Note, however, that larger values of τ_x and smaller values of $f_{\mathrm{C_w}}$, respectively, likewise smooth the simulated precipitation fields. In these cases, the QIRS method used for the evaluation (Sect. 2.4.1) has to be applied carefully.

Table 1. Range of values of the free model parameters used for the calibration of the model.

parameter	minimum	maximum	increment
τ_x	800 s	1500 s	100 s
$f_{\mathrm{C_w}}$	0.5	1.0	0.1
f_{dry}	0.4	1.0	0.1
c_{oro}	0.5	1.0	0.1

The model skill was evaluated using the skill score S according to Taylor (2001) (see Eq. A1 in the Appendix) to determine the best combination of the free model parameter. S relies on the Spearman (1904) correlation coefficient r_{Sp} between the SBM+M simulations and the observations (REGNIE) as well as on the standard deviations σ of both data sets. The skill score S is computed for each day of top200 and each parameter combination. From all realizations, we select the parameter combination that yields the highest median value of S averaged over top200, as the SPM2D should be able to properly represent a broad range of different atmospheric conditions.

4.2 Calibration Results

Applying the method as described above, the highest value for $S = 0.60$ as the median of all top200 events is obtained for the combination of $\tau_x = 1400\,\mathrm{s}$, $f_{\mathrm{C_w}} = 1.0$, $f_{\mathrm{dry}} = 0.4$ and $c_{\mathrm{oro}} = 0.8$. For this combination, the median values of the other quality indices are $r_{\mathrm{Sp}} = 0.39$, $\hat{\sigma}_f = 0.98$, bias $= 6.30\,\mathrm{mm}$, and rmse $= 14.85\,\mathrm{mm}$. The assessed value for τ_x is physically plausible and comparable to other studies with the SBM (e.g., Barstad and Smith, 2005; Caroletti and Barstad, 2010; Kunz, 2011). Considering the slight overestimation of orographic precipitation and the strong overestimation of lee-side drying of the SBM, the values for those adjustments are also physically plausible. Note that the above-identified parameter combination yields the lowest errors only when averaging over all top200 events. Single events are more realistic with another parameter combination, reflecting particularly the unknown, and thus not considered microphysical processes that are decisive for precipitation formation strongly controlled by vertical wind speed, temperature, and moisture profiles. The dependency of microphysical processes on ambient conditions, however, is not relevant when running the model in the stochastic mode as is the objective in this study.

The sensitivity of the skill score S to changes in τ, $f_{\mathrm{C_w}}$, and c_{oro} (Fig. S1, supplements) shows a kind of dipole structure in both cases with the highest values of S along the counter diagonal. Lower values for S are obtained for the shortest (longest) time scales in combination with the highest (lowest) uplift sensitivity or highest (lowest) weighting of R_{oro} in Eq. (1). This means that horizontal precipitation drift over short distances also reduces evaporation, leading to an overestimation of orographic precipitation (and vice versa). This effect has to be considered by adjusting R_{oro}.

4.3 Sensitivity of simulated total precipitation

To demonstrate how variations of atmospheric conditions translate into precipitation, we conduct a sensitivity study with SBM+M using the top200 event set by gradually changing the values of the input parameters. Following Kunz (2011), we perturbed the values of N_{m}^2, q_{v}, U, β, and τ. This is done by multiplying the respective quantity with var_mult increasing linearly from 0.5 to 2.0 in increments of 0.1. Wind direction β is varied in the range of $\pm 30°$ in increments of $5°$. The calibration parameters are set to their optimum values estimated in the previous section. Besides areal mean precipitation, we computed rmse and skill score S for the median of the top200 event set.

Mean precipitation shows a high sensitivity to changes in q_{v}, U and β (Fig. 7). In all cases, precipitation increases (decreases) with increasing (decreasing) values. Lowest sensitivity occurs for β between $\pm 15°$ because of the orientation of the major orographic structures (i.e., the Black Forest) from southwest to northeast. Westerly inflow, prevailing on average, still occurs
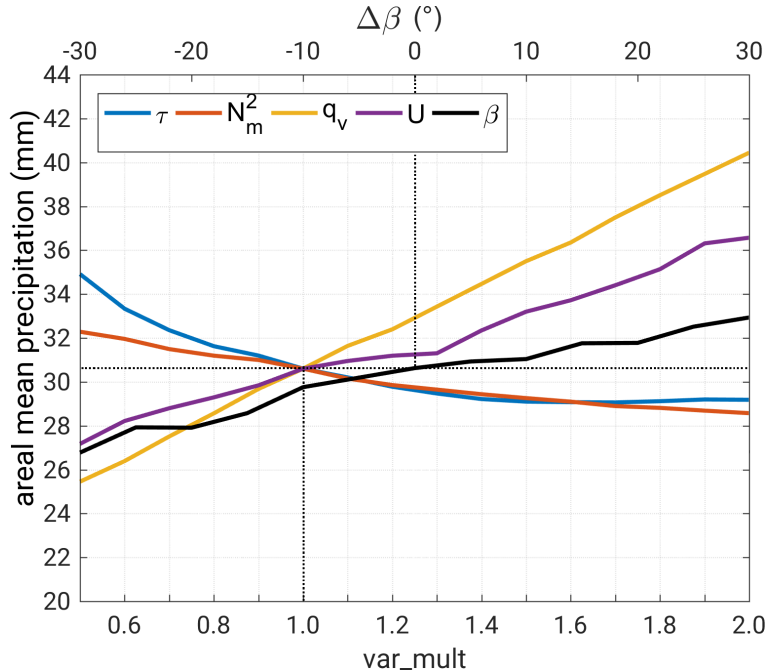
Figure 7. Areal mean precipitation (24-hour totals; median of the top200 event set) as a function of N_m^2, q_v, U, β, and τ perturbed by a multiplicative factor ($0.5 \leq var\_mult \leq 2$) and changed $\Delta\beta$. The dotted lines indicate the values of the reference run.

for small variations of β. For greater shifts ($\Delta\beta > 20°$ or $\Delta\beta < -20°$), when the inflow angle becomes smaller, the sensitivity slightly increases. The changes in the wave regimes and, thus, the location of the updraft may also explain the partly stepwise form of the curves for both β and U. The results for N_m^2 and τ reveal an opposite behavior with an increase of precipitation for smaller values and vice versa. Furthermore, the sensitivity of the SBM+M to changes of these two parameters is much weaker 5   compared to the other parameters.

Qualitatively a similar behavior of the model is found for the medians of rmse and skill score S (Fig. S2). While areal precipitation only provides insights how changes in the ambient parameters feedback into rainfall, rmse and S also consider the spatial distribution. The results for rmse (Fig. S2 a) again reveal the highest sensitivity of the SBM+M to changes in q_v and U. While for $var\_mult > 1$ the sensitivity in terms of rmse is similar to areal precipitation, there is a much higher sensitivity 10   for $var\_mult < 1$. In those cases, orographic precipitation is more detached to the mountain crests resulting in higher totals due to reduced evaporation in the descent regions. Because of the combination of higher totals at different locations, rmse show a higher sensitivity to changes of τ and N_m^2 compared to areal mean precipitation.

The skill score S, on the other hand, is most sensitive to changes in q_v and τ (Fig. S2 b). Regarding N_m^2, S decreases just for very high values of var_mult, while there is almost no sensitivity on β. In all cases, highest S is obtained for the original 15   values of the input parameters, confirming that the model is well calibrated.

4.4 Case Study

After the parameter adjustment, the SBM+M tends to slightly underestimate orographic precipitation, whereas totals over flat or rolling terrain are overestimated. This behavior can be seen for the case study of 31 May 2013 (Fig. 8), a heavy precipitation event that triggered the severe flooding in 2013 (Schröter et al., 2015).

On that day, a pronounced low pressure system with its center over Croatia led to the sustained advection of moist air masses from northerly directions around 20° in combination with synoptic-scale ascent. The Stuttgart sounding showed low stability ($N_m = 0.0055\,\mathrm{s}^{-1}$), high precipitable water ($pw = 24\,\mathrm{kg\,m}^{-2}$), and high wind speed ($U = 20\,\mathrm{m\,s}^{-1}$), which is already an indication of heavy rainfall. Consequently, precipitation totals across the investigation area reached values of 10–100 mm.

Overall, the SBM+M is able to reproduce most of the structures of the observed rain field (Fig. 8), especially the location of the maxima. The observed mean for Baden-Württemberg is $\overline{R}_{\mathrm{obs}} = 33.1$ mm, whereas the simulated mean is $\overline{R}_{\mathrm{mod}} = 37.3$ mm, thus only 12.6 % higher compared to the observations. Maximum values are $R_{\mathrm{max,obs}} = 91.7$ mm and $R_{\mathrm{max,mod}} = 76.3$ mm, respectively, which is a deviation of about 17 %. The area with $R \geq 50$ mm is almost equal with slightly less grid points ($\approx 6\,\%$) in SBM+M. The best agreement is found for the Northern Black Forest as well as the Swabian Jura. Over the northern part of the model domain (north of 49° N) and southwest of Stuttgart, simulated rainfall is substantially higher compared with REGNIE. In contrast, the SBM+M simulates lower totals in the Southern Rhine Valley near and over the mountainous regions of the Southern Black Forest (around Freiburg), especially east of the city of Basel, where lee-side evaporation in the model dominates. The quality indices for that day are $S = 0.62$, $r_{\mathrm{Sp}} = 0.30$, $\hat{\sigma}_f = 0.75$, bias $= 4.44$ mm, and rmse $= 14.82$ mm.
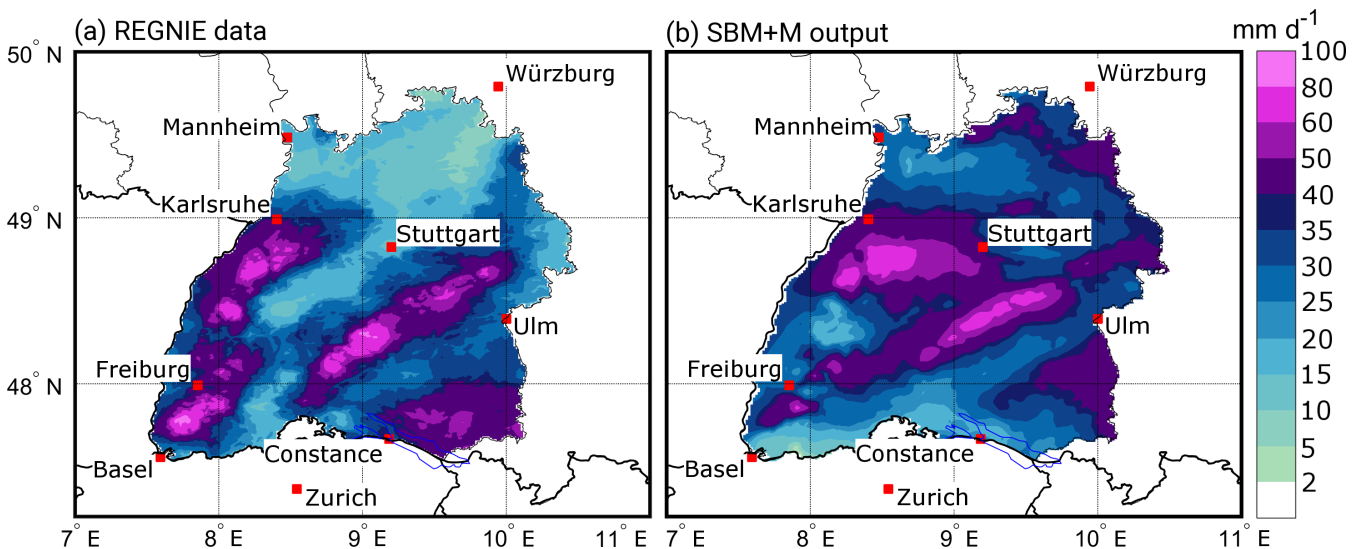
Figure 8. Comparison of (a) REGNIE 24-hour rainfall totals, and (b) SBM+M output for Southwest Germany, exemplary on 31 May, 2013. Note that REGNIE data are available for Germany only. The parametrization in (b) is $\tau_x = 1400\,\mathrm{s}$, $f_{C_w} = 1.0$, $f_{\mathrm{dry}} = 0.4$, and $c_{\mathrm{oro}} = 0.8$. The areas outside of Baden-Württemberg are covered white for better visualization and comparison.

One reason for the discrepancy between observed and simulated precipitation might be the suboptimal location of the Stuttgart sounding used for the model initialization. The sensitivity study as described in Sect. 4.3 for this particular event obtains the best results in terms of the lowest rmse (Fig. 9) for an increase of N_m^2 or τ, whereas in the case of q_v or U, the lowest rmse is obtained when decreasing the original values. Regarding β, the lowest rmse is given for the original value. The
5   highest skill score S, conversely, is reached for increasing U and q_v, and decreasing τ and N_m^2. In the case of β, S continuously decreases from 0.8 for northwesterly inflow to 0.4 for northeasterly winds.
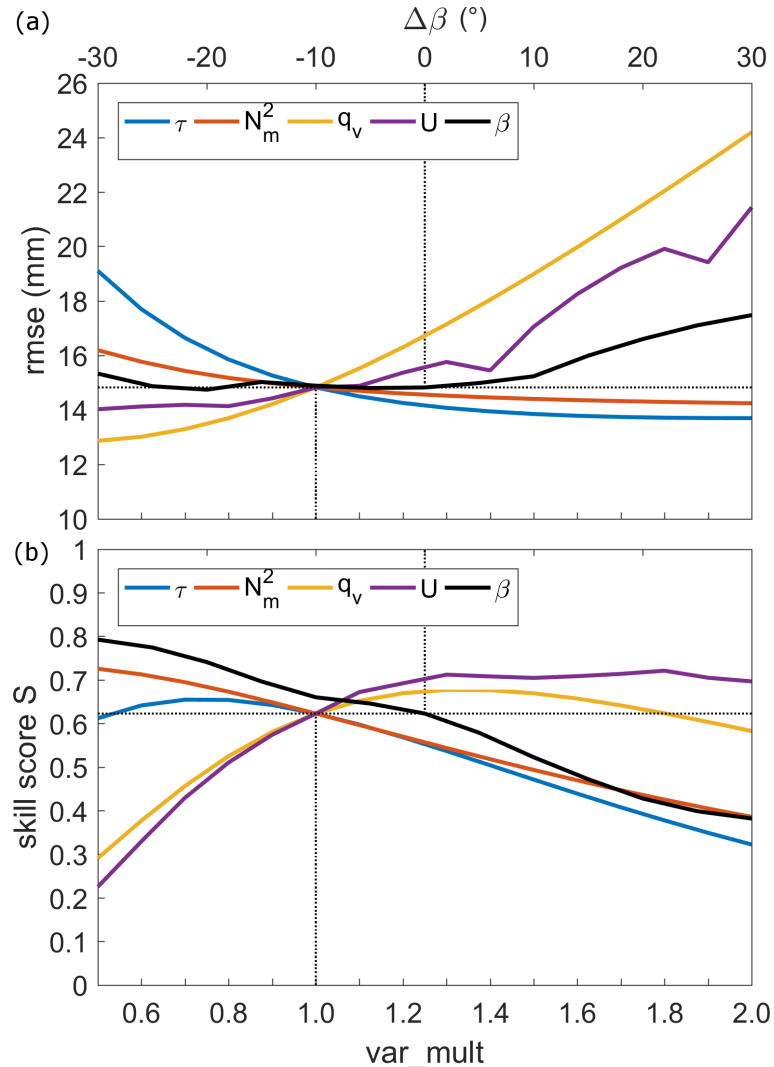
Figure 9. Changes of (a) rmse, and (b) skill score S for perturbed values of N_m^2, q_v, U, β, and τ, with a multiplicative factor (var_mult), and changed $\Delta\beta$, for 31 May, 2013. The dotted lines indicate the values of the reference run.

5 Parameter estimation of the stochastic simulations

5.1 Adjustment of the pdfs

After separating the historic event set into the four main seasons, we estimate for each of the 10 input parameters the pdf that best fits the distribution of the observations (Table 2) by using the least QIRS method (cf. Sect. 2.4.1). From the overall 21 pdfs that were considered, only 12 turned out to be suitable for adjusting the observations. In most of the cases, the generalized extreme value distribution (GEV) with its special realizations of Gumbel (GbD) and Weibull (WbD) distribution appears to be appropriate (26 cases), followed by the inverse Gaussian (IGD) for five parameters and the Gamma distribution (GmD) for three parameters. Especially for flow parameters derived from the soundings, the GEV appears to be the most appropriate (19 out of 28 cases). We had to choose the pdf manually five times due to the alikeness of two pdfs according to the QIRS method.

The input parameters are considered as independent and uncorrelated. To justify this assumption, we performed a correlation analysis of all possible combinations of input parameters using the Spearman (1904) correlation coefficient. A low number of about 16 % of the parameters have a correlation coefficient above ± 0.5, and only 4 % are highly correlated with ± 0.7. Regarding these cases, 90 % show negative correlations with $r \leq -0.5$. However, there are distinct seasonal differences; in some cases correlations are higher in summer than in winter. The highest correlation exists between N_{m}^2 and the lapse rates, which is plausible as both are based on the vertical temperature gradient. Because the SPM2D is less sensitive to N_{m}^2 (c.f. Sect. 4) the effect can be neglected in the model.

Table 2. Estimated best fitting pdfs for event duration (t_{ev}), background precipitation R_∞, and frontal enhancement factor c_{front} derived from REGNIE data (top box); square of saturated Brunt-Väisälä frequency N_{m}^2, wind direction β, horizontal wind speed U, water vapor scale height H_{w}, actual lapse rate γ, saturated moist adiabatic lapse rate Γ_{m}, and condensation rate $\rho_{\mathrm{S_{ref}}}$ derived from sounding data (bottom box); for the pdf aconyms: see Table A1.

model parameter	MAM	JJA	SON	DJF
t_{ev}	GEV	GEV	BSD	NkD
R_∞	WbD	WbD	WbD	WbD
c_{front}	LND	GmD	LND	ND
N_{m}^2	GEV	GbD	GEV	GEV
β	GEV	GEV	GEV	SD
U	HND	IGD	HND	GEV
γ	GEV	GEV	IGD	IGD
Γ_{m}	GEV	IGD	IGD	GEV
H_{w}	GEV	GbD	GEV	LD
$\rho_{\mathrm{S_{ref}}}$	WbD	GEV	WbD	WbD

5.2 Event characteristics

The histogram of the duration t_{ev} for the top200 event set and the corresponding best-fitting pdf, shown exemplary in Fig. 10, illustrated that during JJA, a duration of two to three days dominates with a decreasing probability toward longer periods. During DJF, the distribution is generally shifted to longer events, whereas the probability for single-day events remains roughly unchanged. The maximum of 15 days in DJF represents the longest duration of the top200 event set. Whereas the estimated pdf for the JJA (GEV) has a sharper maximum and a stronger decrease for $t_{\mathrm{ev}} > 3$, the pdf found to best fit the duration in the DJF (NkD) shows a broader range of possible durations. Note that the histogram in the winter shows a large scattering with irregular peaks, making an adjustment of a pdf difficult. For MAM and SON, the results are comparable to those of DJF and JJA, respectively.

Concerning R_{∞}, totals of 20–25 mm d^{-1} are found to most likely occur within a range of 3–37 mm d^{-1} in DJF, 3–50 mm d^{-1} in JJA, and 0–50 mm d^{-1} during the other two seasons (not shown). The corresponding pdfs are listed in Table 2. For the c_{front} parameter, all pdfs have their maximum around 0.7 to 0.8 with a range from 0.4 to 1.4 for most of the seasons (not shown). The distribution in SON (Table 2) descends slower towards higher values (maximum of around 1.6).
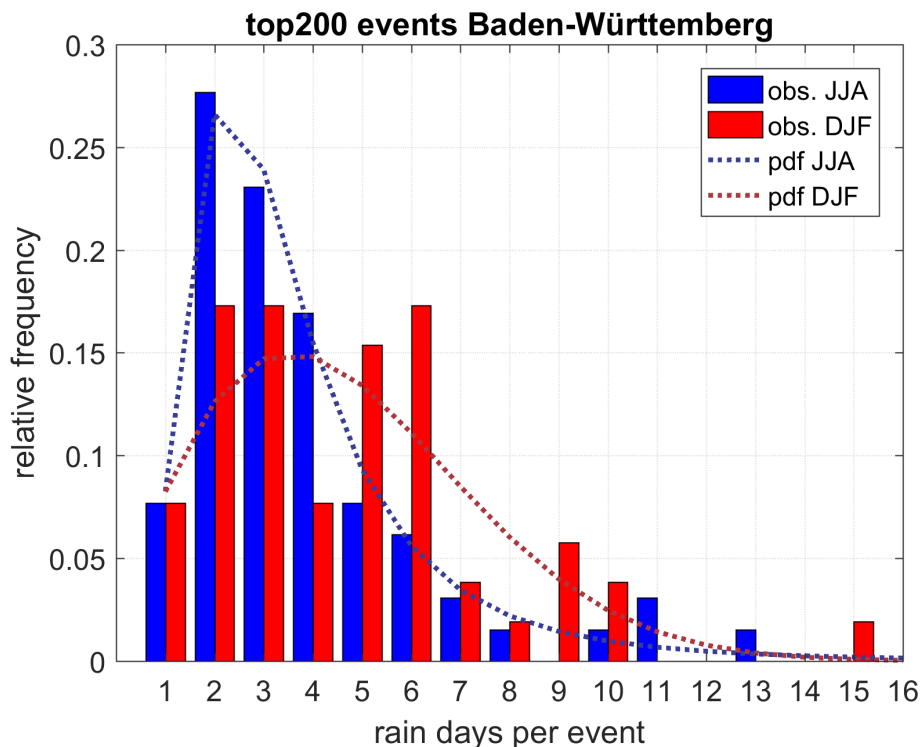
Figure 10. Histogram of top200 event duration for Baden-Württemberg according to REGNIE (bars), and estimated best fitting pdfs (dotted lines) for the summer (blue) and the winter (red).

5.3 Atmospheric parameters

An overview of the range of the seven input parameters of the model is shown as box plots in Fig. 11; the corresponding pdfs are listed in the bottom box of Table 2. In most cases, the atmosphere was slightly stably stratified as represented by positive values of N_m^2 affecting the wave propagation. During JJA, the distribution is shifted toward negative values (unstable; recall that negative values are set to $N_m = 0.0003$ s^{-1}), whereas in DJF, there are almost entirely positive values. Wind direction β, decisive for the spatial distribution of precipitation around the mountains, shows pronounced seasonal differences. More than 90 % of the top200 DJF events have southwesterly to northwesterly winds (240°–300°), with other directions hardly observed. The reason is that northerly flows are usually associated with low temperatures and thus low humidity during DJF. In JJA, the wind direction that occurred most frequently is between 240° and 300° as well. However, all other directions have been observed as well.
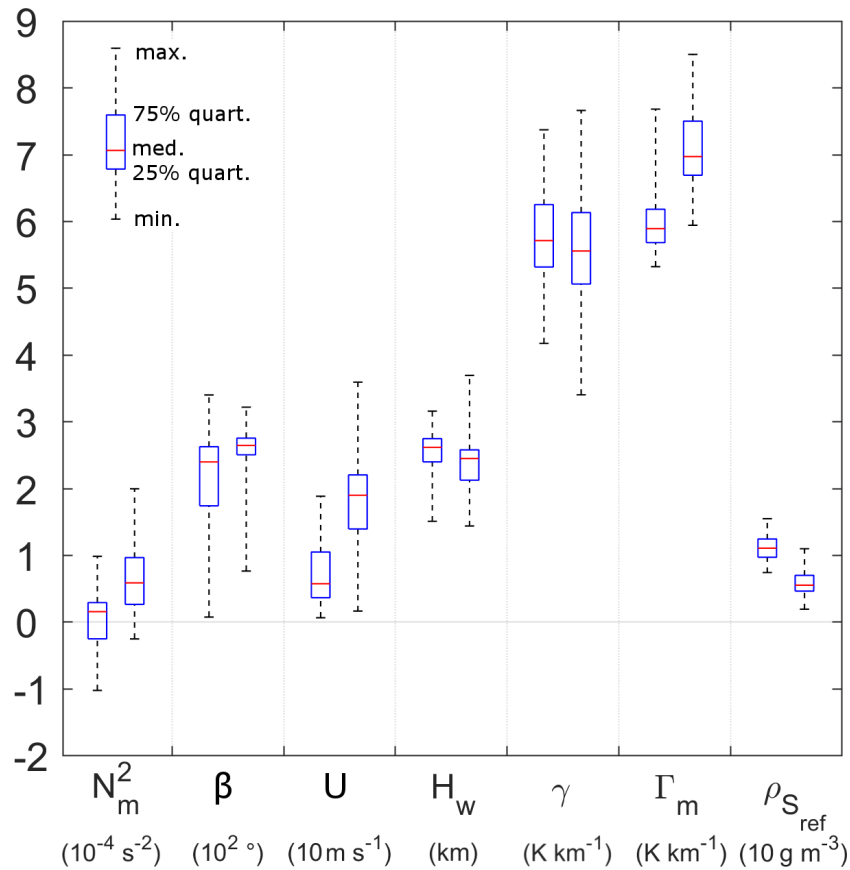
Figure 11. Atmospheric parameters required as input for the SPM2D derived from radiosounding observations at Stuttgart for the top200 events with mean, interquartile distance, minimum, and maximum values; the left box-whisker of each pair represents the summer, the right one represents the winter season. The units for each variable are given in the brackets below the variable names.

Horizontal wind speed U in all cases and all seasons is high, especially during DJF, where reduced moisture is compensated by high velocity to obtain substantial horizontal incoming moisture flow. Median values are 5 and $20\,\mathrm{m\,s^{-1}}$ during JJA and DJF, respectively. Flow parameters related to humidity (H_{w}, $\rho_{\mathrm{S_{ref}}}$) conversely show higher values in JJA, where Γ_{m} is reduced due to the release of latent heat. The quantity γ shows similar medians and interquartile ranges with a broader distribution in DJF.

6   Stochastic event set and model validation

Overall, a total number of $n_{\mathrm{E}} = 10{,}000$ events (equivalent to approx. 31,500 days) have been simulated with the SPM2D in stochastic mode (see Sect. 2.4.2). Therefore, a stochastic set of input variables with the same size as the number of simulation days was created using the estimated pdfs, where the variables can be treated as independent (c.f. Sect. 5.1). For the validation of the SPM2D, we quantified statistical metrics such as return periods, probabilities, and percentiles and evaluated them with observations (REGNIE), CCLM simulations and the SBM+M part. The statistical distribution of the stochastic event set of SPM2D should agree with that of the top200 historic events to a large degree, and more robust results should be notable at the heavy tail (extreme events). The comparison with the SBM+M part is helpful to highlight the quality and necessity of the modifications made to the original SBM. High resolved CCLM simulations are chosen for validation to demonstrate the advantages of a statistical approach for stochastics instead of a dynamical NWP model.

Spatial 24-hour mean values range between 1.2 and 79.7 mm in SPM2D, and 1.3 to 97.0 mm in SBM+M, whereas the maximum for top200 is only 49.6 mm. In total, 128 events (0.4 %) of SPM2D or 724 (2.1 %) of SBM+M yield higher spatial precipitation amounts than the maximum of top200. The CCLM simulations range between 1.8 and 37.6 mm.

Both the median and the 90th-percentile (p90) precipitation fields of the top200 event set and the SPM2D agree well concerning the spatial distribution and the precipitation amounts (Figs. 12 and 13). Significant orographic precipitation enhancement over the Black Forest and Swabian Jura are clearly visible in all data sets. Note that the more detailed structure of the REGNIE data results from the regionalization method and its strong dependency on orography, which should not be over-interpreted. Larger spatial differences between the different realizations mainly appear in the Northern Rhine Valley and to the northeast of the domain for both the median and the p90, whereas for the latter, some differences also arise northeast and southwest of Stuttgart. Nevertheless, all differences are small in the order of a few percent. The SBM+M shows an overestimation of precipitation over mountainous terrain, while the CCLM simulates less precipitation overall for the median. For the p90, major differences appear especially over the rolling terrain.

The areal rainfall of the SPM2D median (Fig. 12) differs only about 3.3 % from the REGNIE top200, whereas that of the SBM+M is about 22.1 % higher. The spatial mean of the CCLM reanalysis is around half of REGNIE, which might be a result of the reduced sample size. The maximum values at any grid point of the median field are about 7 % higher in the SPM2D compared to the REGNIE top200, and about 34 % higher in the SBM+M realization, whereas the CCLM maximum is about 44 % smaller.
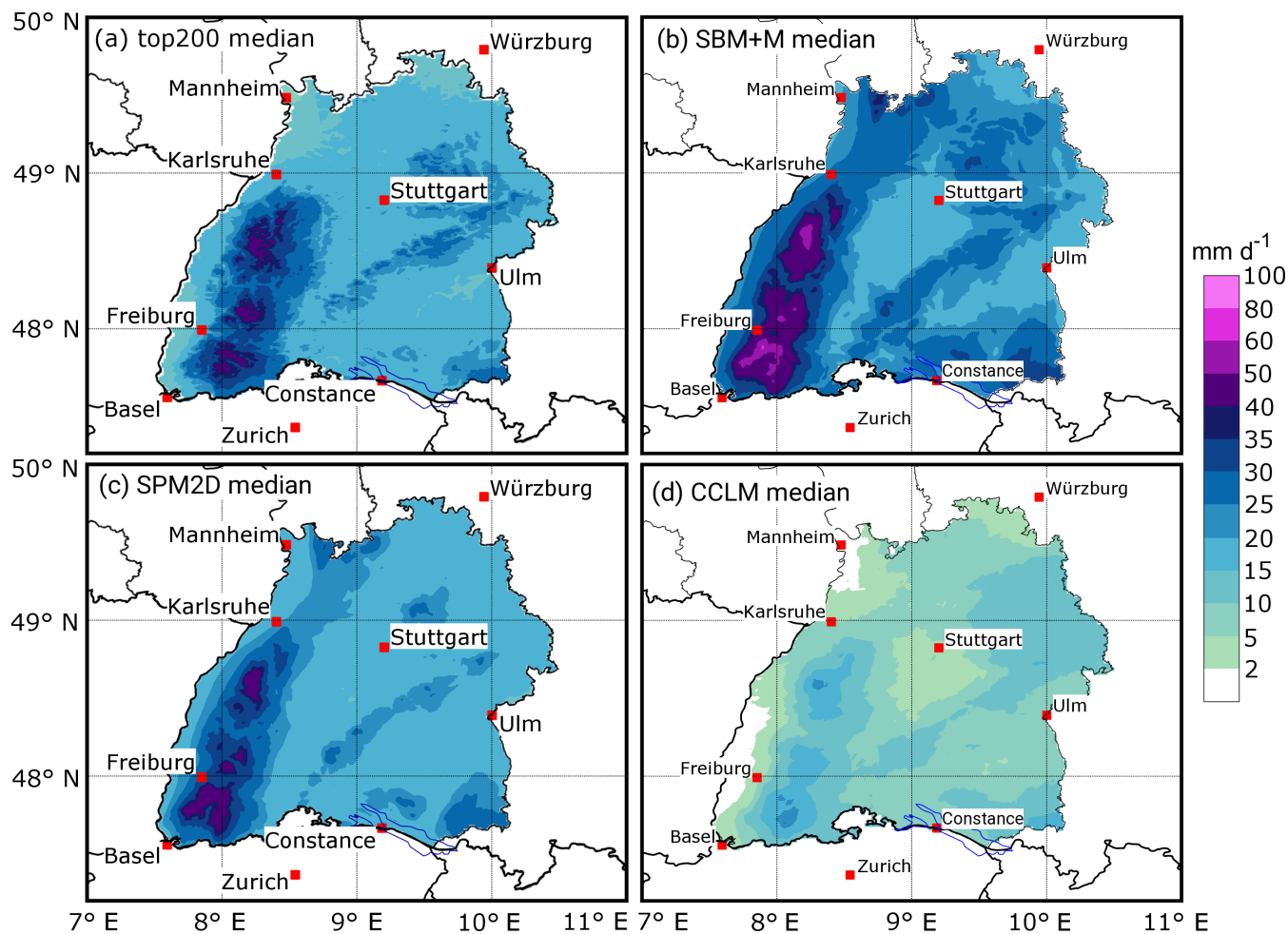
Figure 12. Precipitation fields for the median of (a) the top200 (REGNIE) events, (b) the SBM+M part of the stochastic events, (c) the full SPM2D stochastic event set , and (d) the CCLM simulations of the top REGNIE events.

The areal rainfall for the p90 field (Fig. 13) is about 6.5 % smaller in SPM2D, and about 14 % higher in SBM+M, but about 22 % smaller in CCLM. The maximum values at any grid point of the p90 field is approximately 1 % smaller in SPM2D, and about 22 % higher in SBM+M and 13 % higher in CCLM.

For other percentiles the differences between REGNIE and the SPM2D are very small for both the spatial mean and the maximum precipitation at any grid point in the model domain (Fig. S3 a). The differences become considerable only above the 95th percentile. The SPM2D tends to overestimate lower precipitation amounts because the minimum values at any grid point are higher in the model than in the observations and invert for the 99th percentile only. In contrast, the differences between the SBM+M and REGNIE are considerably larger for maxima, minima and spatial means throughout every percentile. The CCLM reanalysis has a negative deviation for minimum and spatial mean precipitation at all percentiles, whereas for the maximum
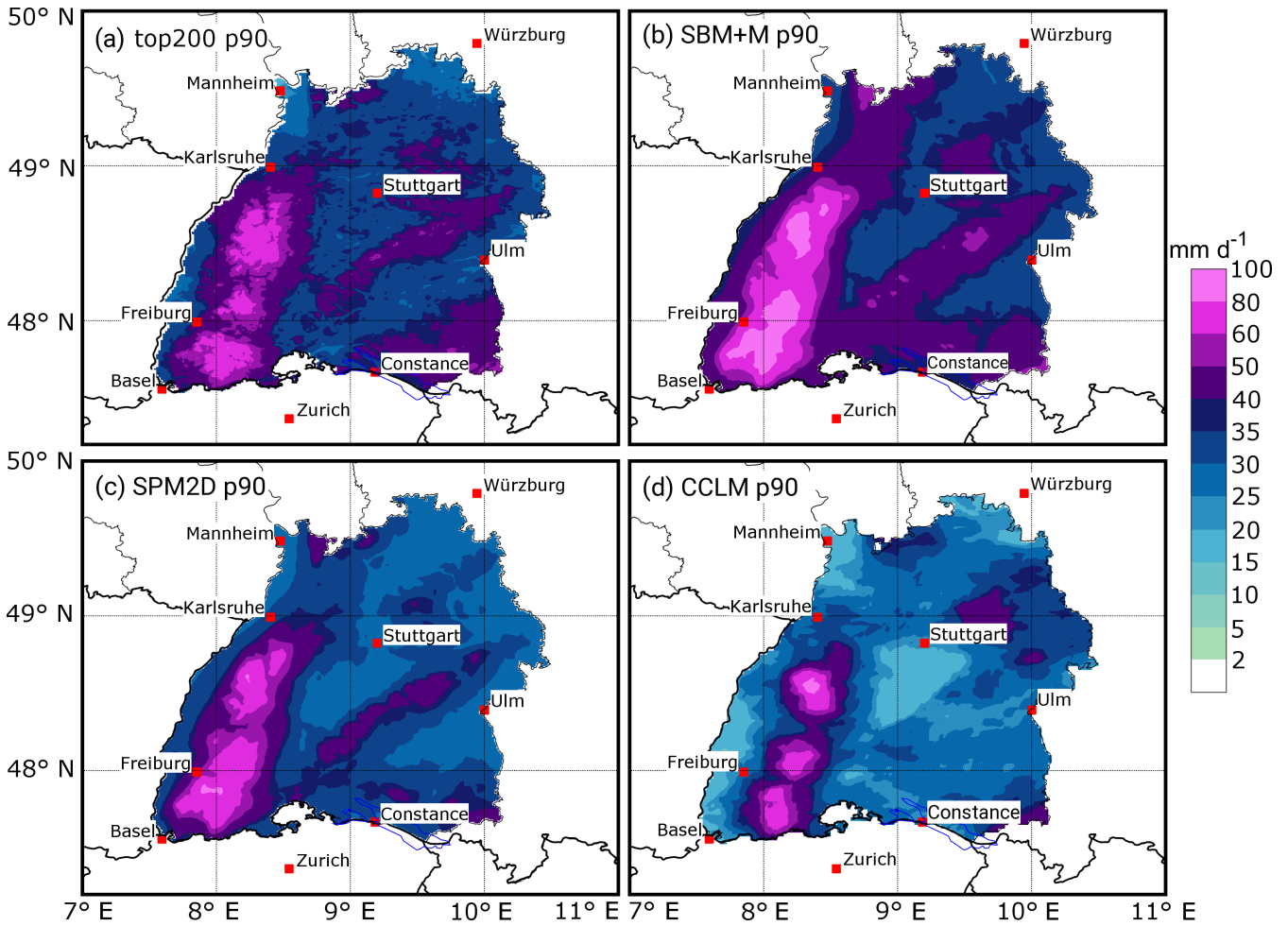
Figure 13. Precipitation fields for the 90th percentile (p90) of (a) the top200 (REGNIE) events, (b) the SBM+M part of the stochastic events, (c) the full SPM2D stochastic event set, and (d) the CCLM simulations of the top REGNIE events.

values there is a marked underestimation for lower percentiles and an overestimation at higher percentiles. At small percentiles, the QIs, such as r_{Sp}, S, or $\hat{\sigma}_f$, have low values due to the overestimation of the SPM2D (Fig. S3 b). The highest skill is reached around the 90th percentile with a slight decrease for higher values, which can be the result of the increasing uncertainties of the observations. Nevertheless, a skill score of around or above 0.8 confirms the reliability of the stochastic simulations.

5   To estimate precipitation distributions for specific return periods, we fit a Gumbel pdf to the annual maximum series of both REGNIE and SPM2D. As it is not possible to directly estimate the time period and a corresponding annual maximum series for the stochastic event set, we count the number of stochastic values exceeding the 99th percentile of observations n_{p99} and

normalize it by the probability of occurrence p_{99}, yielding the new time period:

$$T_{\mathrm{SPM}} = \frac{n_{\mathrm{p}99}}{p_{99}}. \tag{9}$$

After sorting the SPM2D realizations in descending order, we take the first $n_T = T_{\mathrm{SPM}}$ values as the annual series of the SPM2D and estimate a new Gumbel distribution. Using these distributions, we obtain precipitation values for specific return periods for both REGNIE and SPM2D. This method is applied to both the spatial mean values of different areas and for every single grid point.

For a 10-year return period, the SPM2D shows only small differences to REGNIE of less than $\pm 10\%$ over almost the entire area; only in a small region in the southern Black Forest precipitation is higher (Fig. 14 a). The areal mean difference is only 0.6 %. In the case of $T = 200$ years (Fig. 14 b), the slight overestimation in the southern Black Forest area remains almost the same. For this return period, the SPM2D tends to underestimate precipitation, especially in the northern part of BW and in the southeast around Lake Constance. Nevertheless, the differences for most of the grid points are between $\pm 20\%$; areal mean difference is about –10 %. Taking into account the increasing statistical uncertainty for higher return periods, this is still a reasonable result.

On the level of the major river catchments, the differences are small, too. For the Neckar catchment, for example (Fig. 14), which covers about 38 % of BW, the spatial mean deviation is about –0.5 % for $T = 10$ years and –12.7 % for the 200-year return period. Even for catchments containing the area of overestimation in the Southern Black Forest, the spatial mean deviations are between +1 and +4 % for $T = 10$ years and between –2 and –10 % for $T = 200$ years respectively.

Single grid point deviations and the ensuing spatial mean values as described above are sensitive to local conditions and uncertainties in both REGNIE and SPM2D. Hence, we evaluate the model in a similar way by calculating spatial mean precipitation first and then estimate the corresponding return periods (see Appendix A3). Again, the difference between SPM2D and REGNIE is small for entire BW, with slightly lower values from the simulations (Fig. 15a). The distribution of the SPM2D is very close and almost parallel to the estimated observed Gumbel distribution and within the 95 % confidence interval (CI95) estimated with the formula of Maity (2018). Considerable differences between the SPM2D and REGNIE arise only for return periods of $T = 1,000$ years and above, but are still small. For the Neckar catchment, the SPM2D agrees well with the observed distribution for return periods up to $T = 300$ years (Fig. 15 b). For higher return periods, the differences increase, but are still inside the CI95. Similar results can be found for other river catchments (not shown).

7   Summary and Conclusions

We have presented a novel method for estimating the statistics of heavy rainfall based on a stochastic model approach. Total precipitation is calculated from the linear superposition of four different parts: orographic precipitation, synoptic background precipitation, frontal precipitation and precipitation from convection embedded into mainly stratiform clouds. The linear theory of orographic precipitation according to Smith and Barstad (2004), which represents the core of the SPM2D, has been modified using three different calibration parameters to minimize the weaknesses found in previous studies such as the overestimation
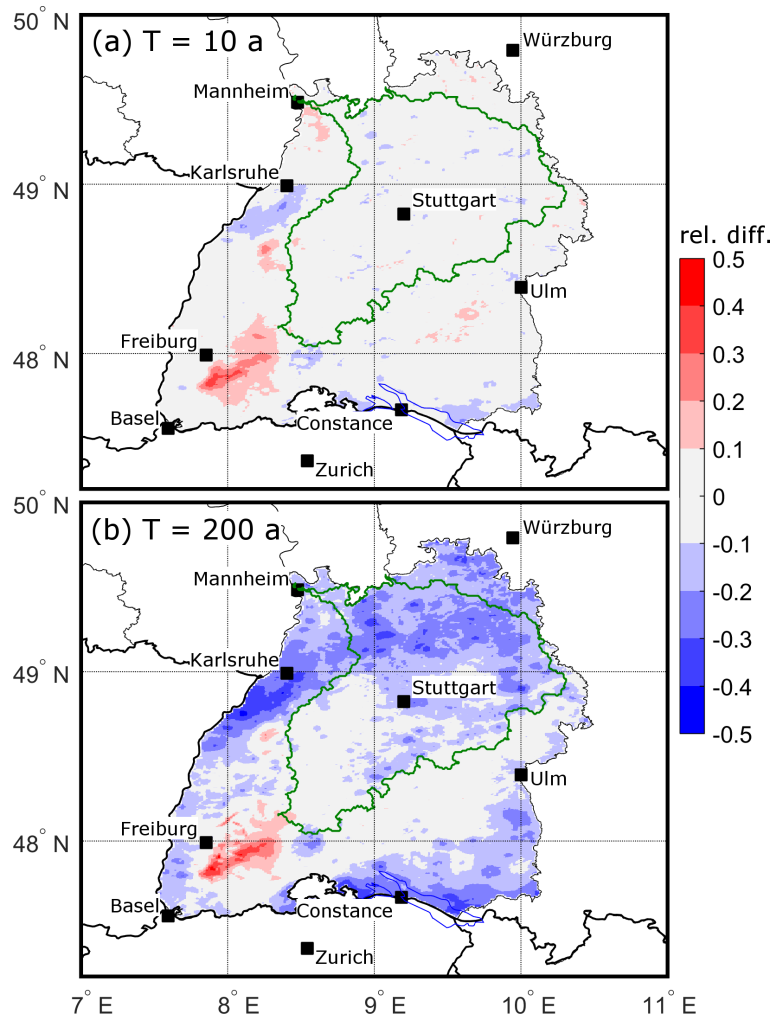
Figure 14. Relative difference of the precipitation amounts for return periods of (a) $T = 10$ years, and (b) $T = 200$ years, according to a Gumbel distribution fitted to the observations (top200) and the SPM2D (see text for further explanation). The Neckar catchment is shown as green contour.

of wave dynamics and, thus, resulting precipitation and evaporation (e. g., Barstad and Smith, 2005; Kunz, 2011). For cross-validation, we calibrated and adjusted the SPM2D to a historic event set of heavy rainfall events (top200; training data). By adjusting appropriate pdfs for all required model parameters, we simulated 10,000 independent stochastic precipitation events (validation data). The results were compared with observations and reanalysis data using different percentiles and return periods.

The focus of the presented investigations was on the Federal State of Baden-Württemberg in Southwest Germany with the striking low-mountain ranges of Black Forest and Swabian Jura. The following main conclusions can be drawn:
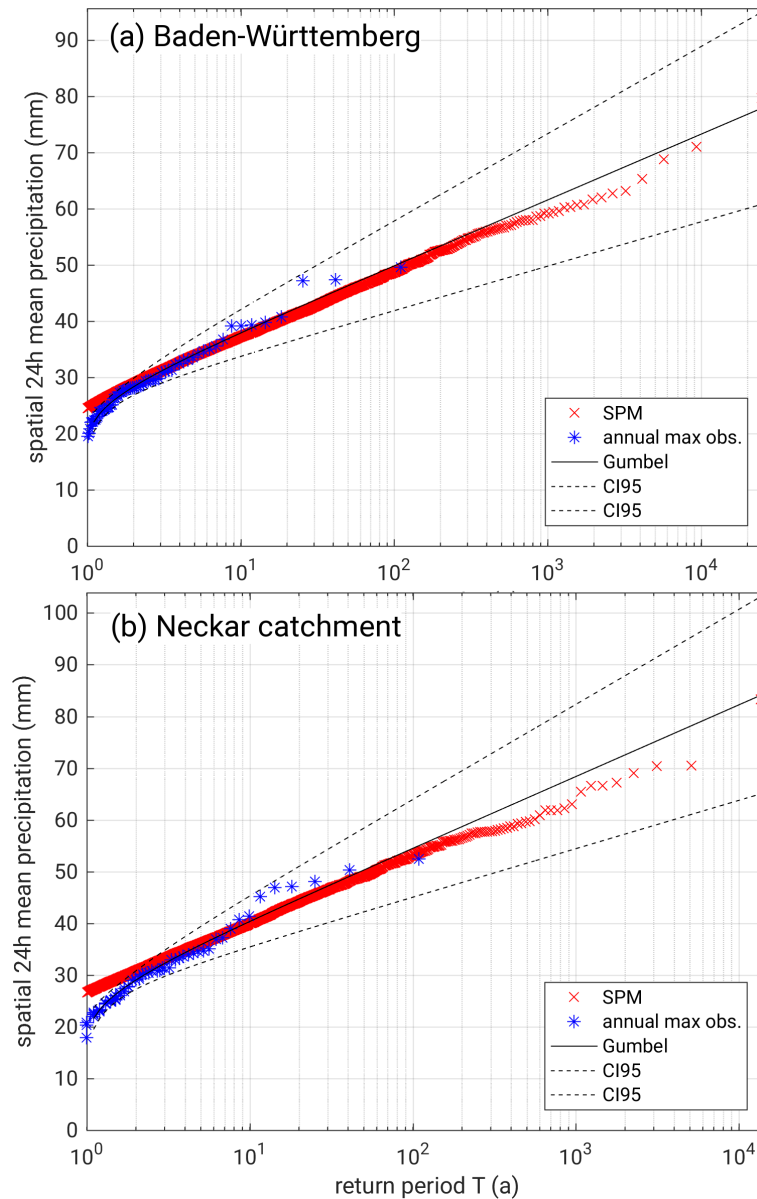
Figure 15. Daily rainfall totals (areal means) as a function of return period T based on the annual maximum series of observations (REGNIE, blue), the corresponding Gumbel distribution including the 95 % confidence intervals (black), and the annual SPM2D series (red) for (a) the Federal State of Baden-Württemberg, and (b) the Neckar catchment.

– The SPM2D has a high skill to simulate both historic and stochastic heavy rainfall events. The simulated precipitation fields and magnitudes are reliable despite the simplified approach of the model initialized by a set of atmospheric variables obtained from radiosoundings. The differences between the SPM2D and REGNIE are small with deviations of less

than 10 %. Local differences, however, may also result from the regionalization procedure of REGNIE, mainly because of the low density of rain gauges over mountainous terrain.

- The comparison of the SPM2D with the underlying linear approach of Smith and Barstad (2004) demonstrates the need for adjustments to the orographic precipitation formulation and for additionally precipitation parts related to frontal systems and embedded convection. The SPM2D with simplified parameterizations for these parts even yields more reliable precipitation fields for a historic event set compared to the sophisticated high-resolution NWP model CCLM.

- The solution of the model equations in Fourier space by an FFT allows for the simulation of a large number of events and to operate the model in stochastic mode. Otherwise, the FFT restricts the model domain to a symmetric equidistant and mesoscale extent.

- The extent of the model domain, furthermore, has to be limited to ensure the validity of the assumption of spatially homogeneous distributed atmospheric conditions and synoptic forcing. This allows, for instance, for the usage of a single vertical profile.

- The presented stochastic approach is easily applicable to other investigation areas. Atmospheric variables for the initialization of the model can be estimated either from radiosoundings as within this study or using reanalysis or data from NWP models. Therefore, it can be applied to any region of the world with similar precipitation characteristics even if there is only a limited number of ground-based observations available.

As shown in our study, the SPM2D is sensitive to perturbations of ambient conditions. Therefore, high-quality input data, especially of the atmospheric parameters, are essential. On the other hand, the sensitivities of precipitation and rmse to changing input parameters is limited in a range of around $\pm 10\,\%$ of the original values, which is usually within the range of uncertainty. Using data of only one sounding station turned out to be sufficient to achieve reliable heavy rainfall fields. As shown by (Kunz, 2011), the differences to another upstream sounding station (Nancy in France) are small, at least in the mean. This, however, applies only for widespread precipitation with duration over several hours to days, which is also the focus of our study. Intermittent or even mainly convectively-driven events cannot be reliably reproduced by our model.

The input parameters can be considered as independent, as just a few cases revealed higher correlations. The sensitivity of the model for these parameters, however, turned out to be week. Additionally, the correlation coefficients between the model input parameters vary among the seasons.

To transfer the method to another investigation area and future risk assessments, just a few steps are necessary: first a proper sample of historical heavy rainfall events. In the next step, the statistics (pdfs) of the prevailing ambient conditions, background precipitation, and duration for the event set have to be calculated. Finally, the non-stochastic part of the SPM2D has to be calibrated by determining appropriate values for the free model tuning parameters.

The output of SPM2D is a certain number of independent heavy precipitation events and not a continuous time series. We have presented a method to convert this to a equivalent time period, which is mostly necessary for risk assessments, by counting the number of days in SPM2D above a defined threshold and normalizing it by the corresponding probability of the

observations. Using this total time span it is possible to estimate the return period of every single event and a corresponding new pdf. The time between two events is assumed as dry period.

The presented SPM2D is part of the project FLORIS (Flood Risk), which represents a novel risk assessment methodology for an entire domain and not only for single catchments usually considered in the insurance industry. Within the framework of this project, the SPM2D was applied to other federal states in central Germany. The modeled precipitation fields are used as input data for hydrological and hydraulic simulations, from which the flood risk can be estimated, for example for a one-in-200-years event required according to the insurance regulation of Solvency II. However, the results of the SPM2D basically can be used for several different applications such as water management or the design of flood protection measures.

8 Data availability

The REGNIE data used in this paper are freely available for research and can be requested at the DWD (doi:10.1127/0941-2948/2013/0436); The sounding data are freely available from the Integrated Global Radiosonde Archive (https://www.ncdc.noaa.gov/data-access/weather-balloon/integrated-global-radiosonde-archive). The required orographic data can be obtained from http://srtm.csi.cgiar.org/ (doi:10.1080/13658810601169899).

Appendix A: Statistical quantities

A1 Probability Density Functions

We used the 20 probability density functions (pdfs) preset in the MATLAB statistical toolbox (MATLAB, 2016) plus the circular von-Mises distribution for wind speed (Mardia and Zemroch, 1975). In total, 17 pdfs were suitable and tested and compared with the observed distribution of each parameter for each of the four seasons (Table A1). Note that the Gumbel (GbD) and Weibull (WbD) distributions are special cases of the generalized extreme value distribution (GEV) and that some pdfs cannot be used due to their ranges.

A2 Skill Score

In this study we use the skill score S introduced by Taylor (2001):

$$S = \frac{4\left(1+r\right)}{\left(\hat{\sigma}_f + \frac{1}{\hat{\sigma}_f}\right)^2 \cdot (1+r_0)}, \tag{A1}$$

where r is the correlation coefficient after Spearman (1904) between modeled and observed precipitation field, r_0 is the maximum attainable correlation, and $\hat{\sigma}_f = \sigma_{\mathrm{mod}} \cdot \sigma_{\mathrm{obs}}^{-1}$ is the normalized standard deviation with the standard deviations of the model (SBM+M) σ_{mod} and observations (REGNIE) σ_{obs}. For $\hat{\sigma}_f \to 1$ and for $r \to r_0$, S approaches unity, which is the best result. Furthermore, Taylor (2001) provided no regulation for the estimation of r_0. Therefore, we set r_0 to the maximum calculated correlation coefficient of all simulations. As it is not guaranteed that this maximum is the actual maximum attainable correla-

Table A1. List of the tested and suitable pdfs preset in the MATLAB statistical toolbox (the short acronyms in brackets are for further orientation).

Birnbaum-Saunders (BSD)	Nakagami (NkD)
Gamma (GmD)	Normal (ND)
Generalized Extreme Value (GEV)	Poisson (PD)
Gumbel (GbD)	Rayleigh (RyD)
Half-Normal (HND)	Rician (RcD)
Inverse Gaussian (IGD)	Stable (SD)
Logistic (LD)	Student's t (StD)
Log-Logistic (LLD)	Weibull (WbD)
Log-Normal (LND)	

tion, we increase r_0 by 10 %, yielding $r_0 = 0.93$. According to Taylor (2001), the use of correlation and standard deviation is more stable compared to rmse or bias.

A3   Return Periods

For the estimation of return periods, the annual maximum series with length T_{max} of the data set is sorted in descending order. Then, the return period T_k of each element x_k of this series is given by $T_k = T_{max} \cdot \mathrm{rk}^{-1}(x_k)$ with the rank $\mathrm{rk}(x_k)$ of element x_k. The first element (highest value) of the annual series of, for example, $T_{max} = 100$ yrs, has a return period of $T_1 = 100$ yrs, the second of $T_2 = 50$ yrs, and so on. For the visualization, the values of T_k were adjusted using the plotting position method of Cunnane (1978).

Competing interests. The authors declare that they have no conflict of interest.

Acknowledgements. The authors thank a local insurance company for funding the project. We also would like to thank the German Weather Service (DWD) and the Integrated Global Radiosonde Archive (IGRA) for providing different observational data sets and CGIAR-CSI for the orographic data. Special thanks go to James Daniell, Andreas Kron and Simon Hoellering from the Karlsruhe Institute of Technology (KIT) for constructive discussions during the project and for valuable suggestions of the model development. We acknowledge support by Deutsche Forschungsgemeinschaft (DFG) and open access publishing fund of KIT. We are grateful to the constructive comments and suggestions of the reviewers that helped to improve the quality of this paper.

References

Barstad, I. and Caroletti, G. N.: Orographic precipitation across an island in southern Norway: model evaluation of time-step precipitation, Q. J. R. Meteorol. Soc., 139, 1555–1565, 2013.

Barstad, I. and Smith, R. B.: Evaluation of an Orographic Precipitation Model, J. Hydrometeorol., 6, 85–99, 2005.

5   Basist, A., Bell, G. D., and Meentmeyer, V.: Statistical relationships between topography and precipitation patterns, J. Climate, 7, 1305–1315, 1994.

Bergeron, T.: On the physics of fronts, Bull. Am. Meteorol. Soc., 18, 265–275, 1937.

Browning, K. A., Pardoe, C. W., and Hill, F. F.: The nature of orographic rain at wintertime cold fronts, Q. J. R. Meteorol. Soc., 101, 333–352, 1975.

10   Cannon, D. J., Kirshbaum, D. J., and Gray, S. L.: Under what conditions does embedded convection enhance orographic precipitation?, Q. J. R. Meteorol. Soc., 138, 391–406, 2012.

Caroletti, G. N. and Barstad, I.: An assessment of future extreme precipitation in western Norway using a linear model, Hydrol. Earth Syst. Sci., 14, 2329–2341, 2010.

Crochet, P., Jóhannesson, T., Jónsson, T., Sigurdsson, O., Björnsson, H., Pálsson, F., and Barstad, I.: Estimating the spatial distribution of
15   precipitation in Iceland using a linear model of orographic precipitation, J. Hydrometeorol., 8, 1285–1306, 2007.

Cross, D., Onof, C., Winter, H., and Bernardara, P.: Censored rainfall modelling for estimation of fine-scale extremes, Hydrol. Earth Syst. Sci. Discuss., https://doi.org/10.5194/hess-2017-437, 2017.

Cunnane, C.: Unbiased plotting positions – a review, J. Hydrol., 37, 205–222, 1978.

Drogue, G., Humbert, J., Deraisme, J., Mahr, N., and Freslon, N.: A statistical-topographic model using an omnidirectional parameterization
20   of the relief for mapping orographic rainfall, Int. J. Climatol., 22, 599–613, https://doi.org/10.1002/joc.671, 2002.

Duckstein, L., Bárdossy, A., and Bogárdi, I.: Linkage between the occurrence of daily atmospheric circulation patterns and floods: an Arizona case study, J. Hydrol., 143, 413–428, 1993.

Durran, D. R. and Klemp, J. B.: On the effects of moisture on the Brunt-Väisälä frequency, J. Atmos. Sci., 39, 2152–2158, 1982.

Durre, I., Vose, R. S., and Wuertz, D. B.: Overview of the integrated global radiosonde archive, J. Climate, 1151, 53–68, 2006.

25   Eliassen, A.: On the vertical circulation in frontal zones, Geophys. Publ., 24, 147–160, 1962.

Fluck, E.: Hail statistics for European countries, Phd thesis, Institute of Meteorology and Climate Research (IMK), Karlsruhe Institute of Technologie (KIT), Karlsruhe, Germany, https://doi.org/10.5445/IR/1000080663, 2018.

Freedman, D. and Diaconis, P.: On the histogram as a density estimator: L2 theory, Zeitschrift für Wahrscheinlichkeitstheorie und Verwandte Gebiete, 57, 453–476, https://doi.org/10.1007/BF01025868, 1981.

30   Fuhrer, O. and Schär, C.: Embedded cellular convection in moist flow past topography, J. Atmos. Sci., 62, 2810–2828, 2005.

Furrer, E. M. and Katz, R. W.: Generalized linear modeling approach to stoachstic weather generators, Clim. Res., 34, 129–144, 2007.

Goovaerts, P.: Geostatistical approaches for incorporating elevation into the spatial interpolation of rainfall, J. Hydrol., 228, 113–129, 2000.

Handwerker, J.: Cell tracking with TRACE3D - a new algorithm, Atmos. Res., 61, 15–34, 2002.

Houze, R. A. and Hobbs, P. V.: Organization and Structure of Precipitation cloud systems, Adv. Geophys., 24, 225–315, 1982.

35   Jiang, Q. and Smith, R. B.: Cloud timescales and orographic precipitation, J. Atmos. Sci., 60, 1543–1559, 2003.

Kållberg, P., Simmons, A., Uppala, S., and Fuentes, M.: The ERA-40 archive. [Revised October 2007], Shinfield Park, Reading, 2004.

Kienzler, S., Pech, I., Kreibich, H., Müller, M., and Thieken, A. H.: After the extreme flood in 2002: changes in preparedness, response and recovery of flood-affected residents in Germany between 2005 and 2011, Nat. Hazards Earth Syst. Sci., 15, 505–526, 2015.

Kirshbaum, D. J. and Durran, D. R.: Factors governing cellular convection in orographic precipitation, J. Atmos. Sci., 61, 682–698, 2004.

Kirshbaum, D. J. and Smith, R. B.: Temperature and moist-stability effects on midlatitude orographic precipitation, Q. J. R. Meteorol. Soc., 134, 1183–1199, https://doi.org/10.1002/qj.274, 2008.

Koutsoyiannis, D., Kozonis, D., and Manetas, A.: A mathematical framework for studying rainfall intensity-duration-frequency relationships, J. Hydrol., 206, 118–135, 1998.

Kunz, M.: Characterisitics of Large-Scale Orographic Precipitation in a Linear Perspective, J. Hydrometeorol., 12, 27–44, 2011.

Kunz, M. and Wassermann, S.: Moist dynamics and sensitivity of orographic precipitation to changing ambient conditions in an idealised perspective, Meteorol. Z., 20, 199–215, 2011.

Lalas, D. P. and Einaudi, F.: On the stability of a moist atmosphere in the presence of a background wind, J. Atmos. Sci., 30, 795–800, 1973.

Laube, N.: personal correspondence, Phd thesis, Institute of Meteorology and Climate Research (IMK), Karlsruhe Institute of Technologie (KIT), Karlsruhe, Germany, 2018.

Maity, R.: Statistical Methods in Hydrology and Hydroclimatology, Springer Nature Singapore Pte Ltd., https://doi.org/10.1007/978-981-10-8779-0, 2018.

Mardia, K. V. and Zemroch, P. J.: Algorithm AS 86: The Von Mises Distribution Function, Journal of the Royal Statistical Society. Series C (Applied Statistics), 24, 268–272, 1975.

Marra, F., Morin, E., Peleg, N., Mei, Y., and Anagnostou, E. N.: Intensity–duration–frequency curves from remote sensing rainfall estimates: comparing satellite and weather radar over the eastern Mediterranean, Hydrol. Earth Syst. Sci., 21, 2389–2404, https://doi.org/10.5194/hess-21-2389-2017, 2017.

MATLAB: MATLAB and Statistics Toolbox Release 2016b, (version 9.1), The MathWork Inc., Natick, Massachusetts, USA, http://de.mathworks.com/help/, last visited 10 August 2017, 2016.

Mohr, S. and Kunz, M.: Recent trends and variabilities of convective parameters relevant for hail events in Germany and Europe, Atmos. Res., 123, 211–228, 2013.

MunichRe: NatCatSERVICE, natcatservice.munichre.com/, accessed: 28 Sept 2017, 2017.

Neykov, N. M., Neytchev, P. N., and Zucchini, W.: Stochstic daily precipitation model with a heavy-tailed component, Nat. Hazards Earth Syst. Sci., 14, 2321–2335, https://doi.org/10.5194/nhess-14-2321-2014, 2014.

Palutikov, J. P., Brabson, B., Lister, D. H., and Adcock, S. T.: A review of methods to calculate extreme wind speeds, Meteorol. Appl., 6, 119–132, 1999.

Peleg, N., Marra, F., Fatichi, S., Paschalis, A., Molnar, P., and Burlando, P.: Spatial variability of extreme rainfall at radar subpixel scale, J. Hydrol., 556, 922 – 933, https://doi.org/10.1016/j.jhydrol.2016.05.033, 2018.

Petrow, T., Zimmer, J., and Merz, B.: Changes in the flood hazard in Germany through changing frequency and persistence of circulation patterns, Nat. Hazards Earth Syst. Sci., 9, 1409, 2009.

Piper, D., Kunz, M., Ehmele, F., Mohr, S., Mühr, B., Kron, A., and Daniell, J.: Exceptional sequence of severe thunderstorms and related flash floods in May and June 2016 in Germany-Part 1: Meteorological background, Nat. Hazards Earth Syst. Sci., 16, 2835, 2016.

Rauthe, M., Steiner, H., Riediger, U., A., M., and Gratzki, A.: A Central European precipitation climatology - Part I: Generation and validation of a high-resolution gridded daily data set (HYRAS), Meteorol. Z., 22, 235–256, 2013.

Richardson, C. W.: Stochastic Simulation of Daily Precipitation, Temperature, and Solar Radiation, Water Resour. Res., 17, 182–190, 1981.

Rockel, B., Will, A., and Hense, A.: The regional climate model COSMO-CLM (CCLM), Meteorol. Z., 17, 347–348, 2008.

Schröter, K., Kunz, M., Elmer, F., Mühr, B., and Merz, B.: What made the June 2013 flood in Germany an exceptional event? A hydro-meteorological evaluation, Hydrol. Earth Syst. Sci., 19, 309–327, 2015.

Smith, R. B.: Linear theory of stratified hydrostatic flow past an isolated mountain, Tellus, 32, 348–364, 1980.

Smith, R. B.: Hydrostatic airflow over mountains, Adv. Geophys., 31, 1–41, 1989.

Smith, R. B. and Barstad, I.: A Linear Theory of Orographic Precipitation, J. Atmos. Sci., 61, 1377–1391, 2004.

Spearman, C.: The Proof and Measurement of Association between Two Things, The American Journal of Psychology, 15, 72–101, 1904.

Taylor, K. E.: Summarizing multiple aspects of model performance in a single diagram, J. Geophys. Res., 106, 7183–7192, 2001.

Uhlemann, S., Thieken, A. H., and Merz, B.: A consistent set of trans-basin floods in Germany between 1952-2002, Hydrol. Earth Syst. Sci., 14, 1277, 2010.

Wanner, H., Rickli, R., Salvisberg, E., Schmutz, C., and Schüepp, M.: Global climate change and variability and its influence on alpine climate-concepts and observations, Theor. Appl. Climatol., 58, 221–243, 1997.

Wilks, D. S.: Statistical Methods in the Atmospheric Sciences, vol. 91 of *International Geophysics Series*, Academie Press, San Diego, California, USA, 2nd edn., 2006.